Delamination in collisional orogens: Thermomechanical modeling

K. Ueda,[1,2] T. V. Gerya,[2,3] and J.-P. Burg[2]

Received 9 January 2012; revised 1 May 2012; accepted 1 July 2012; published 9 August 2012.

[1] Modes of mantle delamination in collision zones are discussed in the light of 2D numerical modeling. Freely evolving thermomechanical models take into account phase changes in the mantle and melting in the crust. Distinct modes are identified, in which orogens undergo mantle delamination concurrently or after collision. Delamination propagates along the Moho of the subducted plate together with the retreating trench, provided that slab pull is sufficient and that the meta-stability of the crust-lithospheric mantle interface is overcome. Topography is an instantaneous response to delamination and migrates with the focused and localized separation between crust and lithospheric mantle (delamination front). Early exhumation of high-pressure rocks is followed by exhumation of high-temperature, partially molten rocks. Convective stabilization of delamination outlasts slab break-offs and impedes renewed build-up of mechanically strong lithospheric mantle by static cooling. Parameter studies investigate the sensitivity of delamination to the age of the subducted oceanic plate, the collision rate, the mantle rheology, and explore the effects of melting and sedimentation. Mantle flow patterns that form around delamination and subduction are sensitive to and often limited by the semi-permeable 670 km spinel-perovskite transition, demonstrating that phase-changes are essential factors. Delamination may account for the formation of complex boundary zones between continents, such as between Africa and Europe in the Mediterranean, where transient compression and extension, the lack of mantle lithosphere, and the exhumation of high-grade metamorphic core complexes are features also obtained in our modeling results.

Citation: Ueda, K., T. V. Gerya, and J.-P. Burg (2012), Delamination in collisional orogens: Thermomechanical modeling, *J. Geophys. Res.*, *117*, B08202, doi:10.1029/2012JB009144.

1. Introduction

[2] The meta-stability of tectonic plates, which consist of positively buoyant crustal and negatively buoyant lithospheric mantle layers, plays an important role in driving plate tectonics and affects the pattern of upper mantle convection. The negative buoyancy of Phanerozoic (and possibly Proterozoic) lithosphere [*Poudjom Djomani et al.*, 2001] allows for its foundering into the mantle at localized subduction zones, a mechanism recognized to account for first order plate forces, for the incitement of mantle flow, and ultimately for planetary heat and material exchange [*Wyllie*, 1988; *Conrad and Lithgow-Bertelloni*, 2006; *Tackley*, 2008]. The effective buoyancy antagonism between crust and lithospheric mantle implies an inherent potential of separation along their boundary. This potential is little understood and currently underestimated within the context of evolving convergence-subduction-collision zones, where separation is necessary as lithospheric slabs sink into the mantle, and where the natural exposure of high-pressure, low-temperature (HP-LT) rocks gives evidence for rapid exhumation of formerly subducted crust.

[3] In this study, we investigate the continuous evolution of a convergent plate boundary from subduction and collision to delamination and eventual collapse of the evolving orogen. We use a setup that numerically reproduces self-consistent modes of delamination evolving from early and late stages of collisional orogeny, while only the initiation of early subduction is prescribed by a weak lithospheric zone. Correlations between subduction zone/orogen style and the modes of delamination are studied by varying selected parameters. The subsequent evolution of the plate boundary is examined with a long-term perspective; end-member states are compared to potential geological analogues. Following previous approaches of coupled thermomechanical and petrological modeling, we employ models that take into account competing plasticity, viscous creep, and Peierl's creep, thermodynamically consistent phase changes, and a large model box to account for flow in the mantle.

2. Background

[4] Geological examples for the removal of lithospheric mantle, in particular by delamination, have been put forward

[1]Department of Earth Science, University of Bergen, Bergen, Norway.
[2]Department of Earth Sciences, ETH Zürich, Zürich, Switzerland.
[3]Geology Department, Moscow State University, Moscow, Russia.

Corresponding author: K. Ueda, Department of Earth Sciences, ETH Zürich, Sonneggstr. 5, CH-8092 Zürich, Switzerland. (kosuke.ueda@erdw.ethz.ch)

0148-0227/12/2012JB009144

for a variety of tectonic cases [e.g., *Bird*, 1979; *Channell and Mareschal*, 1989; *Nelson*, 1992; *Seber et al.*, 1996; *Rey et al.*, 1997; *Sperner et al.*, 2004; *Saleeby and Foster*, 2004; *Göğüs and Pysklywec*, 2008b; *Jacobs et al.*, 2008; *Wallner and Schmeling*, 2011]. It is increasingly accepted that such a removal of the mantle has a first order impact on the geological exposure in zones of plate thickening. Delamination is invoked as the deep cause of various asynchronous phenomena, including uplift and high topography, extension, elevated heat flow, high temperature-low pressure (HT-LP) metamorphism, or the granitoid magmatism of collapsing orogens [e.g., *Kay and Kay*, 1993; *Jacobs et al.*, 2008; *Wallner and Schmeling*, 2011; *Ueda et al.*, 2012]. Delaminaton is also thought to account for a change in seismic reflectivity of the lower crust and the Moho [e.g., *Nelson*, 1992; *Leech*, 2001]. It is therefore of interest to predict, from dynamically consistent models, surface and sub-surface observables that are characteristic for delamination and that support discrimination between lithospheric delamination and other processes.

[5] Several processes such as slab break-off [*Sacks and Secor*, 1990; *Gerya et al.*, 2004; *Baumann et al.*, 2010; *Duretz et al.*, 2011], externally forced splitting by lateral insertion of rigid tectonic wedges [e.g., *Ellis*, 1988; *Cook et al.*, 1998; *Tsumura et al.*, 1999; *Moore and Wiltschko*, 2004], and convective thinning [*Houseman et al.*, 1981; *Spohn and Schubert*, 1982; *Houseman and Molnar*, 1997; *Conrad*, 2000; *Göğüs and Pysklywec*, 2008a] are known to have the potential to separate negatively buoyant material from tectonic plates in zones of convergence and thickening. However, only delamination is localized and propagates along the crust-lithosphere boundary, thus opening asthenospheric windows of considerable width through the lithospheric mantle [*Bird*, 1979; *Bird and Baumgardner*, 1981; *Göğüs and Pysklywec*, 2008b]. Following the terminology in material sciences, we use delamination to describe a planar separation along the layering of a composite, where the bonding of materials with different properties, like it is the case in tectonic plates, can fail [e.g., *Evans and Hutchinson*, 1984].

[6] *Bird* [1979] recognized the similarity of planar delamination and subduction in terms of (incited) flow surrounding the foundering lithosphere. Subsequent thermomechanical simulations of delamination have highlighted the importance of a convecting upper mantle [*Schott and Schmeling*, 1998; *Morency and Doin*, 2004]. Delamination was found to propagate as "peeling" of the lithosphere, with only a small area delaminating at a given time [*Bird and Baumgardner*, 1981]. As with other tectonic processes [e.g., *Ueda et al.*, 2008; *Nikolaeva et al.*, 2010; *Burov and Cloetingh*, 2010], while the forcing and the principal localization are unambiguous, the circumstances of delamination initiation are not well known. The meta-stability of the crust-lithospheric mantle boundary can principally be overcome and exploited if means are provided to decouple and separate the layers. A critical condition for this separation is the presence of strength minima, potentially occurring not only along the Moho in spatial coincidence with the buoyancy contrast, but also below or above [*Kusznir and Park*, 1986; *Meissner and Mooney*, 1998; *Schott et al.*, 2000; *Brown and Phillips*, 2000; *Seno*, 2008].

[7] Initiation of delamination has proven to be a difficult modeling problem, so that simulations were performed with *ab initio* assumptions of weak zones to facilitate a controlled separation of the lithospheric mantle from the crust [e.g., *Bird*, 1979; *Göğüs and Pysklywec*, 2008b; *Valera et al.*, 2011]. These assumptions have pre-empted to relate the characteristic development of a delaminating collision zone to the preceding orogenic history. Delamination observed in numerical and analogue models of collision zones and methodological advances allow further steps to refine the numerical treatment [*Gerya and Yuen*, 2003, 2007; *Boutelier et al.*, 2004; *Gerya et al.*, 2008; *Faccenda et al.*, 2009; *Duretz et al.*, 2011; *Göğüs et al.*, 2011]. Improvements concern (1) the dynamically unconstrained development of models from as early as possible, ideally not imposing any initial weakness for delamination to start and develop from subduction models; (2) the thermodynamical implementation of a layered mantle (resulting in reduced permeability of transition zones for sinking slabs) in order to capture as accurately as possible the characteristics of upper mantle flow; and (3) consideration of phase changes, hydration and melting in order to account for reduced coupling at the plate interface and to generate crustal characteristics comparable to geological observations (e.g., partially molten rocks).

3. Method

3.1. Model Formulation

[8] We use a modified version of the two-dimensional finite difference code I2VIS [*Gerya and Yuen*, 2003; *Duretz et al.*, 2011]. The thermal problem is solved by diffusion on a non-uniform Eulerian grid, non-diffusive Lagrangian advection, and accounts for latent, radioactive, adiabatic, and shear heating. Interpolation of properties from markers to nodes [cf., *Schmeling et al.*, 2008] is achieved by inverse-distance weighted bilinear arithmetic averaging [*Gerya and Yuen*, 2003]. Under an extended Boussinesq approximation, conservative formulations for an incompressible viscous fluid are used and combined with plasticity by limiting creep viscosity in relation to plastic yield stress and strain rate invariants [*Gerya and Yuen*, 2007]. The viscous creep combines diffusion and dislocation creeps that compete with low-temperature Peierls creep [*Kameyama et al.*, 1999]. The importance of accounting for the Peierls mechanism in fast, thermally unequilibrated convergent settings has been demonstrated [e.g., *Duretz et al.*, 2011], as it can significantly reduce the integrated strength of the lithosphere. A quasi-free surface is achieved by a low viscosity and low density top layer [*Schmeling et al.*, 2008]. In our models, this layer has a constant viscosity of 10^{19} Pa·s, but includes air and water with their respective densities of 1 and 1000 kg/m^3. Given the chosen layer thickness and viscosity, this layer approximates a freely evolving internal lithological surface at least for long time-scales [*Crameri et al.*, 2012]. Shortcomings of this approach are negligible because of the large model dimensions compared to the topography and an imposed limitation of topographic slopes; furthermore, these shortcomings are accepted because of the long observation time-scales of this study. The surface is modified by a gross-scale erosion-sedimentation law at a fixed rate of 0.1 mm/a for rocks below or above a prescribed erosion/sedimentation level (10 km) [e.g., *Duretz et al.*, 2011]. The surface is advected in the same way as lithology and rock properties (rheological, thermal) on the Lagrangian markers. The

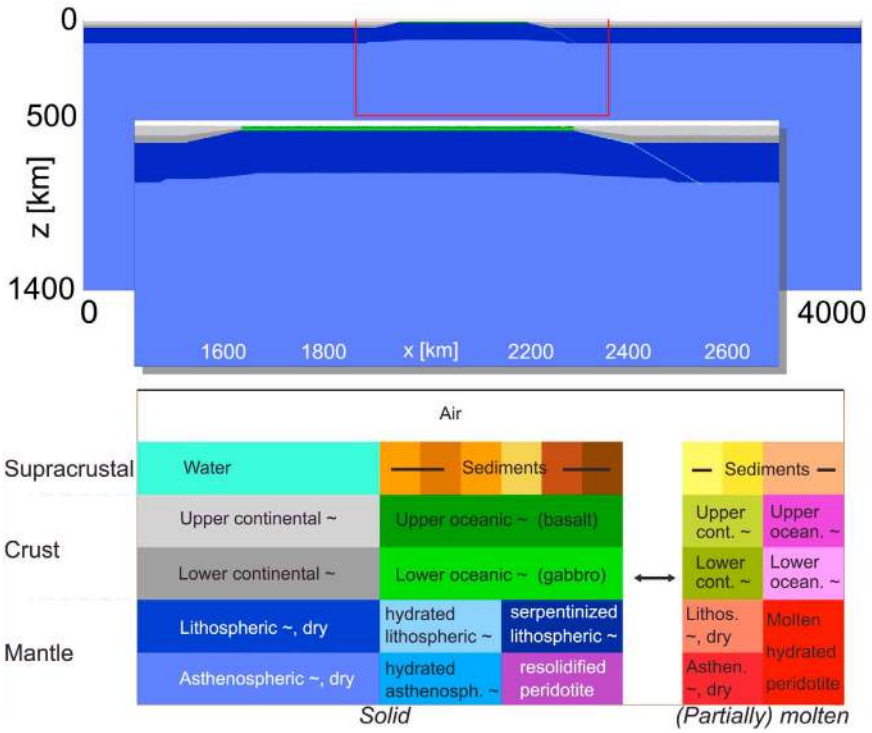

Figure 1. Initial model setup and lithological representation. The thickness of the lithospheric mantle for the oceanic plate is a varied parameter controlled by thermal age. Lithologies that undergo melting or partial melting change color as shown.

thermodynamical-petrological model relates rock properties to Eulerian P-T-f_{H2O} conditions and minimizes Gibbs free energy by changes of phase and partial melting, which are fed back into the thermal problem [*Burg and Gerya*, 2005]. Water is treated both as depth-dependent pore water content and as water bound in hydrous minerals that are subject to thermodynamical stability calculations, allowing excess water (dehydration) and its movement as fluid markers. Melting was switched off in some models to unravel its dynamic effects. Rheological and thermal equations [*Gerya and Yuen*, 2003, 2007; *Duretz et al.*, 2011] are listed in the appendix with details for the implementation of fluid exchange and migration, and for melting processes [*Sizova et al.*, 2010].

[9] The mechanical boundary conditions are free-slip on top, right and left sides and a vertically permeable lower boundary (prescribing normal velocity) that satisfies an external free slip condition [e.g., *Burg and Gerya*, 2005; *Ueda et al.*, 2008]. Thermal boundaries prescribe zero heat flux across the lateral boundaries, 273 K at the top of the model box, and 2244 K at an external, 1500 km deep lower boundary. A thermal boundary at the internal lithological surface is emulated by a high thermal conductivity (20 W/m·K) in the top low-viscosity layer and by resetting temperatures for all air and water markers to 273 K at each time step. Mantle is treated as lithospheric mantle if it is cooler than 1300 K (homologous to ca. 0.85 · $T_{solidus}$ for olivine at 1 GPa) for depths <200 km; below that depth, mantle that originated from the lithosphere retains (for tracking purposes; Figure 1) its darker color even if it is physically treated as asthenosphere.

[10] The thermodynamical and rheological properties used for the different materials are given in Table 1.

[11] For the visualization of results, marker properties such as lithology are interpolated (infinite-norm averaging) onto a regular visualization grid of 1 km resolution, while the irregular marker distribution corresponds to an average resolution of advected properties of ca. 0.3 km. Sediments are represented with cyclically changing colors (every 100 time steps), without a corresponding change in properties.

3.2. Setup and Initial Conditions

[12] The collision zone is modeled in a 4000 × 1000 km model box on an irregular grid of 1361 × 351 nodes with a refined grid spacing of 1 km in the center, between 1600 and 2600 km in x-direction, and between 0 and 200 km in y-direction. The lithology is defined on ca. 11.6 million markers. Tectonic plates are represented as two continents separated by 700 km of oceanic lithosphere (Figure 1). The top low-viscosity layer of the model simulates 10 km of atmosphere, above 2 km of water covering the oceanic domain. Continents comprise 20 km of upper felsic crust (wet quartzite; Table 1) and 15 km of lower crust (Plagioclase-An_{75} [*Ranalli*, 1995]). The initial thickness of the subcontinental lithospheric mantle is 125 km unless otherwise stated (Table 2). The oceanic plate is represented by 3 km of upper basaltic crust, and 5 km of lower gabbroic crust; the thickness of the lithospheric mantle is a function of chosen initial age (homogeneous for the entire plate width) and calculated using an oceanic geotherm. This produces a simplified plate of homogeneous thickness and thermal structure. While it does not represent lateral differences in age and thickness that would be expected for an intervening

Table 1. Rheological and Thermal Properties of Modeled Rock Materials[a]

Material	Flow Law	n	η ($Pa^n s$)	E_A (kJ/mol)	C (Mpa)	$\sin(\phi)$	$T_{solidus}$ (K)	$T_{liquidus}$ (K)	H_R ($\mu W/m^3$)	H_L (kJ/kg)	C_p (J/kg)	k (W/m·K)	ρ (kg/m^3)x
Sediments	Wet quartzite	2.3	$1.97\cdot10^{17}$	$1.54\cdot10^{5}$	1	0.15	$P < 1200$ MPa: $889 + \frac{17900}{P+54} + \frac{20200}{(P+54)^2}$; $P > 1200$ MPa: $831 + 0.06\cdot P$	$1262 + 0.009\cdot P$	1.5	300	1000	$0.64 + \frac{807}{T+77}\cdot e^{(0.00004\cdot P)}$	2600
Upper cont. crust	Wet quartzite	2.3	$1.97\cdot10^{17}$	$1.54\cdot10^{5}$	1	0.15	$P < 1200$ MPa: $889 + \frac{17900}{P+54} + \frac{20200}{(P+54)^2}$; $P > 1200$ MPa: $831 + 0.06\cdot P$	$1262 + 0.009\cdot P$	1	300	1000	$0.64 + \frac{807}{T+77}\cdot e^{(0.00004\cdot P)}$	2700
Lower cont. crust	Plagioclase (An_{75})	3.2	$4.80\cdot10^{22}$	$2.38\cdot10^{5}$	1	0.15	-//-	$1423 + 0.105\cdot P$	0.25	380	1000	$1.18 + \frac{474}{T+77}\cdot e^{(0.00004\cdot P)}$	2800
Upper oceanic crust	Wet quartzite	2.3	$1.97\cdot10^{17}$	$1.54\cdot10^{5}$	1	0	$P < 1600$ MPa: $973 - \frac{70400}{P+354} + \frac{7.78\cdot10^{7}}{(P+354)^2}$; $P > 1600$ MPa: $935 + 0.0035\cdot P + 6.2\cdot10^{-6}\cdot P^2$	$1423 + 0.105\cdot P$	0.25	380	1000	$0.64 + \frac{807}{T+77}\cdot e^{(0.00004\cdot P)}$	3000
Lower oceanic crust	Plagioclase (An_{75})	3.2	$4.80\cdot10^{22}$	$2.38\cdot10^{5}$	1	0.6	-//-	$1423 + 0.105\cdot P$	0.25	380	1000	$1.18 + \frac{474}{T+77}\cdot e^{(0.00004\cdot P)}$	3000
Mantle	Dry olivine	3.5	$3.98\cdot10^{16}$	$5.32\cdot10^{5}$	1	0.6	$1394 + 0.133\cdot P_{MPa} - 5.1\cdot10^{-6}\cdot P^2_{MPa}$	$2073 + 0.114\cdot P$	0.022	-//-	1000	$0.73 + \frac{1293}{T+77}\cdot e^{(0.00004\cdot P)}$	3300
Hydrated mantle	Wet olivine	4	$5.01\cdot10^{20}$	$4.70\cdot10^{5}$	1	0	$P < 1600$ MPa: $973 - \frac{70400}{P+354} + \frac{7.78\cdot10^{7}}{(P+354)^2}$; $P > 1600$ Mpa: $935 + 0.0035\cdot P + 6.2\cdot10^{-6}\cdot P^2$	$2073 + 0.114\cdot P$	0.022	300	1000	$0.73 + \frac{1293}{T+77}\cdot e^{(0.00004\cdot P)}$	3200
Molten sedim. & cont. cr.	-//-	1	$5.00\cdot10^{14}$	0	1	0	-//-	-//-	1.5	-//-	1500	-//-	2400
Molten oceanic crust	-//-	1	$1.00\cdot10^{13}$	0	1	0	-//-	-//-	0.25	-//-	1500	-//-	2900
Molten peridotite	-//-	1	$1.00\cdot10^{13}$	0	1	0	-//-	-//-	0.022	-//-	1500	-//-	2900
Reference	1	1	1	1			2	2	3	3,4		5	3

[a] η: reference viscosity; n: stress exponent; E_A: activation energy; C: plastic cohesion; ϕ: angle of internal friction; H_R: radiogenic heat production; H_L: latent heat; Cp: isobaric heat capacity; k: thermal conductivity; $\rho 0$: density. Constant for all materials: $a = 3\cdot10^{-5}\ K^{-1}$, $b = 1\cdot10^{-3}\ MPa^{-1}$. References: 1: *Ranalli* [1995]; 2: *Schmidt and Poli* [1998]; 3: *Turcotte and Schubert* [2002]; 4: *Bittner and Schmeling* [1995]; 5: *Clauser and Huenges* [1995].

Table 2. Parameters of Conducted Numerical Experiments[a]

Model			Input Parameters						
			Convergence Rate		Age of Oceanic	Rheology			
Number	Particular Setting	Melting Enabled	vx_L (cm/a)	vx_R (cm/a)	Lithosphere (a)	V_A Lith 10^{-6} (m^3/mol)	V_A Mantle 10^{-6} (m^3/mol)	Result	Figures
01		n	4	4	8e7	8	8	syn-collisional delamination	
02		n	2.5	2.5	8e7	8	8	failure/arrest	
03		n	1	1	1.1e8	8	8	syn-collisional delamination	
04		n	1	1	9.5e7	8	8	failure/arrest	
05		n	4	4	5.5e7	8	8	syn-collisional delamination	
06		n	3.3	3.3	6e7	8	8	syn-collisional delamination	
07		n	4	4	4.5e7	8	8	failure/arrest	
08		n	2.5	2.5	1e8	8	8	syn-collisional delamination	
09		n	4	4	6e7	8	8	syn-collisional delamination	
10		n	5	5	4e7	8	8	failure/arrest	
11		n	5	5	8e7	8	8	syn-collisional delamination	11
12		n	5	5	6e7	8	8	syn-collisional delamination	
13		n	5	5	1e8	8	8	syn-collisional delamination	
14		n	5	5	2e7	8	8	failure/arrest	
15		y	5	5	6e7	8	8	failure/arrest	5a–5c
16		y	5	5	6e7	8	8	syn-collisional delamination	
17		y	5	5	8e7	8	8	syn-collisional delamination	
18		y	5	5	1e8	8	8	syn-collisional delamination	2, 3, 10–12
19		y	4	4	8e7	8	8	syn-collisional delamination	
20		y	2.5	2.5	8e7	8	8	syn-collisional delamination	
21		y	4	5	8e7	8	8	syn-collisional delamination	
22		y	5	4	8e7	8	8	syn-collisional delamination	
23		y	0.5	0.5	8e7	8	8	syn-collisional delamination	
24	v_e = 1 mm/a	y	1	1	5e7	8	8	failure/arrest	
25	v_e = 1 mm/a	y	1	1	6e7	8	8	failure/arrest	
26		y	5	5	4e7	8	8	failure/arrest	
27		y	5	5	2e7	8	8	failure/arrest	
28		y	5	5	5e7	8	8	failure/arrest	
29		y	2.5	2.5	6e7	8	8	syn-collisional delamination	
30		y	1	1	7e7	8	8	syn-collisional delamination	
31		y	4	4	5e7	8	8	failure/arrest	
32		y	5	5	5.5e7	8	8	failure/arrest	
33		y	4	4	6e7	8	8	syn-collisional delamination	
34		y	1	1	6.5e7	8	8	syn-collisional delamination	
35		y	3.33	3.33	6e7	8	8	failure/arrest	
36		y	3.33	3.33	6.5e7	8	8	syn-collisional delamination	
37		y	2.5	2.5	7e7	8	8	syn-collisional delamination	
38		y	0.5	0.5	6.5e7	8	8	syn-collisional delamination	
39		y	5	5	8e7	9	9	syn-collisional delamination	13
40		y	5	5	8e7	12	12	failure/arrest	
41		y	5	5	8e7	9	8	syn-collisional delamination	
42		y	5	5	8e7	10	10	failure/arrest	
43		y	5	5	8e7	11	11	failure/arrest	
44		y	5	5	8e7	9.5	9.5	syn-collisional delamination	
45		y	5	5	1e8	9.5	9.5	syn-collisional delamination	
46		y	5	5	1e8	10	10	syn-collisional delamination	
47		y	5	5	6e7	8.5	8.5	failure/arrest	
48		y	2.5	2.5	8e7	9	9	syn-collisional delamination	
49		y	2.5	2.5	8e7	10	10	transient syn-collisional delamination	
50		y	4	4	8e7	9.5	9.5	syn-collisional delamination	
51		y	5	5	1e8	11	11	transient syn-collisional delamination	
52		y	2.5	2.5	8e7	11	11	failure/arrest	5d–5f
53		y	4	4	8e7	10	10	syn-collisional delamination	
54		y	5	5	7e7	9	9	failure/arrest	
55		y	4	4	8e7	11	11	post-collisional delamination	
56		y	2.5	2.5	8e7	12	12	failure/arrest	
57		y	1	1	8e7	12	12	post-collisional delamination	4, 10–12
58		y	5	5	1e8	11.5	11.5	failure/arrest	
59		y	2.5	2.5	8e7	10.75	10.75	failure/arrest	
60		y	1	1	8e7	11.5	11.5	post-collisional delamination	
61		y	2.5	2.5	8e7	11.5	11.5	post-collisional delamination	
62		y	4	4	8e7	10.5	10.5	transient syn-collisional delamination	
63		y	4	4	8e7	11.5	11.5	post-collisional delamination	
64		y	1	1	8e7	11	11	post-collisional delamination	
65		y	1.75	1.75	8e7	11.5	11.5	post-collisional delamination	
66		y	1.75	1.75	8e7	12	12	post-collisional delamination	

Table 2. (continued)

Model			Input Parameters						
			Convergence Rate		Age of Oceanic	Rheology			
Number	Particular Setting	Melting Enabled	vx_L (cm/a)	vx_R (cm/a)	Lithosphere (a)	V_A Lith 10^{-6} (m^3/mol)	V_A Mantle 10^{-6} (m^3/mol)	Result	Figures
67		y	1.75	1.75	8e7	11	11	failure/arrest	
68		y	1	1	8e7	10.5	10.5	failure/arrest	
69		y	3.33	3.33	8e7	11	11	failure/arrest	
70		y	5	5	8e7	10.5	10.5	transient syn-collisional delamination	
71		y	5	5	8e7	11.5	11.5	failure/arrest	
72		y	4	4	8e7	12	12	failure/arrest	
73		y	1	1	8e7	10.25	10.25	syn-collisional delamination	
74		y	2.5	2.5	8e7	10.5	10.5	transient syn-collisional delamination	
75	v_f, $v_m = 3{\cdot}10^{-10}$ m/s	y	5	5	8e7	8	8	syn-collisional delamination	
76	$v_f = 3{\cdot}10^{-10}$ m/s	y	5	5	8e7	8	8	syn-collisional delamination	
77	$v_m = 3{\cdot}10^{-10}$ m/s	y	5	5	8e7	8	8	syn-collisional delamination	
78	$v_e = 3$ mm/a	y	5	5	8e7	8	8	syn-collisional delamination	
79	$v_s = 10^{-7}$ mm/a	y	5	5	8e7	8	8	syn-collisional delamination	
80	$v_s = 10^{-10}$ mm/a	y	5	5	8e7	8	8	syn-collisional delamination	
81	dct	y	5	5	6e7	8	8	transient stagnation and subsequent delamination	7,11
82	lcg	y	1	1	8e7	12	12	syn-collisional delamination	9
83	lcg	y	5	5	1e8	8	8	syn-collisional delamination	

[a] vx_L, vx_R – left, right continent convergence rate; V_A lith, V_A mantle – olivine activation volume for lithospheric mantle and asthenosphere. Particular model parameters: dct – different continent thicknesses, left mantle 125 km, right 150 km (all other cases 125 km); v_f, v_m – modified maximum vertical migration velocity for fluids and molten rocks [cf. *Faccenda et al.*, 2009], v_e – modified erosion rate; v_s – modified sedimentation rate; lcg – lower crustal rheology felsic granulite [*Ranalli*, 1995].

spreading center, this setup provides a conceptually simple way to relate slab length, mass, and age for dynamic considerations. A thin weak zone of hydrated mantle (2 km wide) is placed along the contact of the oceanic lithosphere with the continent on the far (right) side of the increasing x-coordinate in order to initiate subduction on a numerically and visually tractable site. The comparatively narrow width of this zone provides an initial weakening site, while ensuring that its material will not significantly contaminate the developing subduction channel and determine its physical properties. A weak zone along the plate contact can be thought of as tectonic inheritance from previous plate boundary activity, or as an emulation of the gravitational instability and subduction initiation at a passive margin that may be subjected to sediment loading [e.g., *Cloetingh et al.*, 1982; *Regenauer-Lieb et al.*, 2001; *Nikolaeva et al.*, 2010].

[13] Continental plates are initialized with a temperature of 273 K at their surface and 1617 K on the bottom of the lithosphere, with a consecutive, quasi-adiabatic gradient of 0.5 K/km in the subjacent mantle.

[14] Initial convergence, which is assumed to be provided by external plate forces, is imposed at internal nodes within both plates at with fixed convergence rates, until the oceanic plate is consumed in the subduction zone. The rate condition is then lifted and the system evolves further responding to internal forces. No mass is introduced or removed at the boundaries.

4. Results

[15] Eighty-three models simulated the development and dynamics of collision zones. Three major modes of long-term development have been identified: (1) delamination coeval with subduction and collision ("syn-collisional delamination"), (2) delamination post-dating collision ("post-collisional delamination"), and (3) preservation of the orogenic lithosphere without delamination ("arrested development"). In addition to these three end-members, we present a mixed mode in which the plate boundary stagnates for tens of Ma before delaminating, further referred to as "transitional stagnation." Sensitivity studies were performed with variations in the parameters of oceanic age (i.e., lithosphere thickness), convergence rate at which each continent is moved individually toward the center of the model, and increase of depth-dependent viscosity increase expressed in terms of activation volume V_A of olivine. V_A corresponds to viscous "resistance" to free slab movements and was varied well within the range of experimental results [e.g., *Mei and Kohlstedt*, 2000] and close to the value of $9.5 \pm 7 \cdot 10^{-6}$ m^3/mol reported by *Durham et al.* [2009]. At low pressures, our explored V_A range of $8–12 \cdot 10^{-6}$ m^3/mol can be mapped to small effective viscosity changes (<a factor of 2); they reach one order of magnitude difference for pressures of 20 GPa and above.

[16] The geometry of the subduction zone and thermal and geometrical characteristics of the collisional orogen are sensitive to these parameters, as reported below, and can be linked to the outlined modes of delamination. The sensitivity of delamination to additional parameters such as suppression of melting, mobility of fluids and (partially) molten rocks, thickness of the continental lithosphere, rates of erosion and sedimentation, and different crustal rheologies was tested with a few experiments, but has not been mapped systematically.

4.1. Syn-collisional Delamination

[17] In 40 models with convergence rates between 5 and 0.5 cm/a, oceanic ages between 60 and 110 Ma, and activation

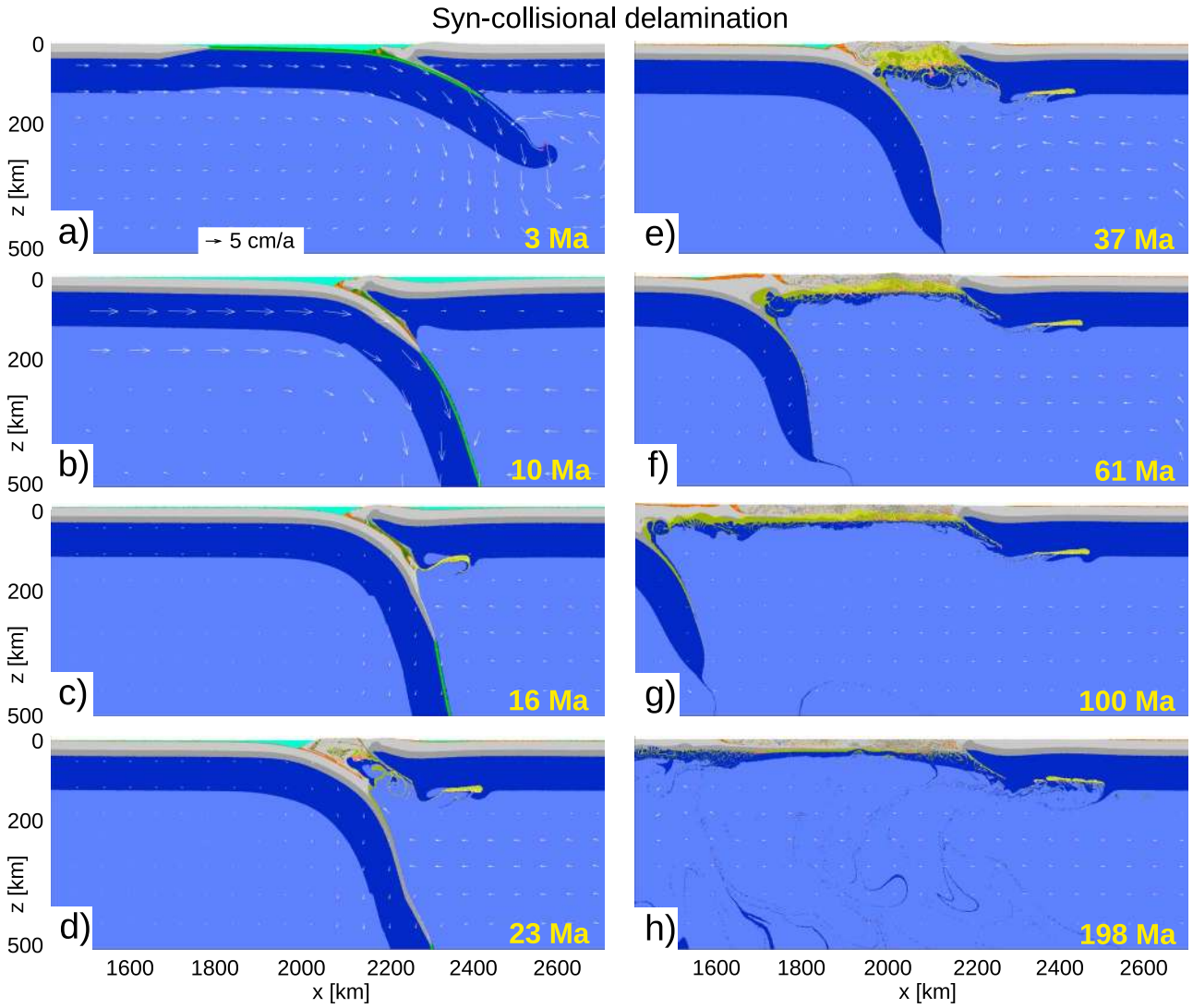

Figure 2. Syn-collisional delamination (model 18). Fast convergence produces steep subduction and a weakened plate interface. (a) Initial subduction continues and even accelerates until the initial (b) 200–300 km of continental crust are subducted. (c) High temperatures due to exposure to asthenosphere reduce viscosity and mobilize first the upper crust, and later the lower crust (Figures 2d and 2e). (d) Mobilized crust migrates into the subduction channel; weak coupling facilitates widening of the channel and intrusion of asthenosphere (Figure 2d). The steepened slab retreats, tearing the weak plate interface (Figure 2d), and (e–h) leading a propagation tip of delamination. Basally heated crust melts partially (Figures 2e–2g), raises isostatically (Figures 2e and 2f), and extends (Figures 2f–2h). Slab break-off occurs between Figures 2e and 2f.

volumes between 8 and 11 $\cdot$ 1^{-6} m^3/mol, delamination occurs immediately after the onset of continental collision (Figure 2, reference model 18; age of oceanic lithosphere 80 Ma, convergence rate = 5 cm/a, $V_A = 8 \cdot 10^{-6}$ m^3/mol). After consumption of the ocean and ending of the imposed rate condition, net convergence of the plates continues under internal dynamics (Figure 2b), leading to further subduction while the overriding plate becomes immobile. The slab steepens. The crust of the subducted continent reaches depths >200 km (Figure 2b). An initial topographic high develops in a narrow (ca. 100 km wide) zone without elevated temperatures (partial melting) or significant crustal thickening.

[18] Contact with the asthenosphere due to deep subduction thermally weakens the subducted continental crust. The lowered-viscosity (ca. 10^{19} Pa·s), buoyant upper crust migrates upwards up to about 10 km depth in a return flow along the subduction channel (Figure 2c). At the same time, the slab rolls back and the trench retreats. Subducting and overriding plates decouple along the low-viscosity subduction channel which widens and is intruded by uprising asthenosphere (Figure 2d). The lower continental crust of the subducting plate, exposed to asthenosphere after the earlier extrusion of upper crust, is also thermally weakened and flows upwards along the slab-asthenosphere contact to coalesce with a layer of partially molten crust in the center of the

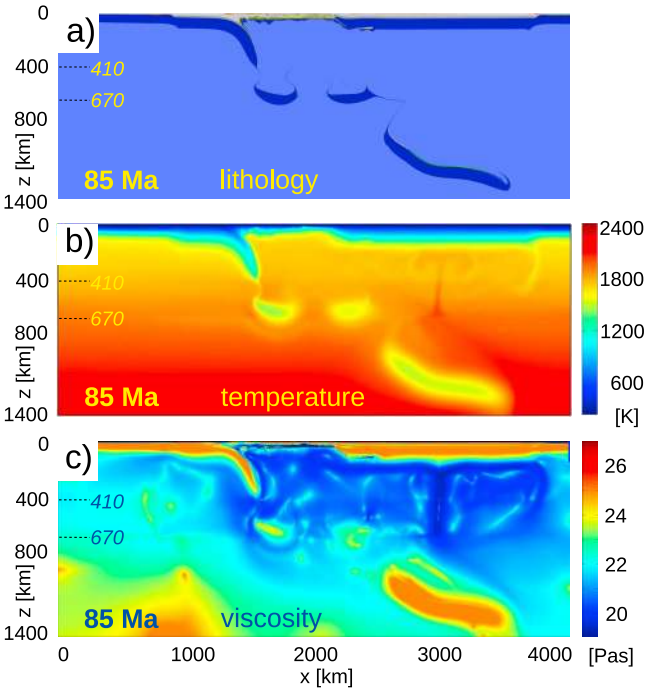

Figure 3. Large-scale evolution of orogenic delamination (model 18). (a) Delamination propagates regardless of slab break-off. Fragments of lithospheric mantle may or may not penetrate the phase transition at 670 km. Note that melting is not modeled below 400 km (oceanic remnant). (b) Temperature - thermal effect of delamination. The thermal layering and latent heat exchange at phase transitions at 410 and 670 km is visible; accommodation of slab passage by upward counterflow through the endothermic spinel-perovskite transition sparks a hot thermal instability. (c) Viscosity - moving mantle has lower effective viscosity. Note low-viscosity zone coinciding with thermal upwelling in Figure 3b.

spreading subduction channel. The mobilized slab crust underplates the continental crust that lies directly over the developing asthenospheric window. This crustal underplating leads to crustal thickening and high topography (Figures 2d and 2e) in the developing orogen. Basal heating causes partial melting in the orogenic crust within few Ma after exposure to asthenosphere.

[19] After opening of the asthenospheric window (Figure 2d), the convective flow around the retreating, further sinking and breaking-off slab is sustained (Figure 2f). As part of this convection pattern, the asthenosphere below the delaminated crust remains in steady convection. The retreat of the crust-free subducting slab continues despite repeated break-off (before Figures 2e–2g, respectively; the result of three break-offs is shown in Figure 3), and is part of a continuous convective movement of the upper mantle. The change of properties due to phase transitions in the mantle impels different levels at which broken slabs sink (Figure 3); the first, usually large fragment penetrates through the spinel-perovskite transition at ca. 670 km. Smaller fragments stay afloat (Figure 3a). This conditional permeability controls the scale of convection patterns in the upper mantle.

[20] In the reference model 18 (Figure 2), oceanic closure happens ca. 6.7 Ma after the start of the experiment. Collision continues until ca. 13 Ma; delamination and return flow of subducted continental crust is observed at ca. 16 Ma (Figure 2c), and exposure of non-subducted crust to the opening asthenospheric window, with incipient continental melting, begins at ca. 27 Ma. Lateral propagation of delamination is initially ca. 1–1.2 cm/a fast, but slows down to ca. 0.3 cm/a at ca. 80 Ma; a new lithospheric mantle starts to form below the delaminated crust at ca. 200 Ma. Replenishment is slow; the half-thickness of the initial lithosphere is regained at ca. 300 Ma. The total width of the asthenospheric window reaches 800–1000 km.

4.2. Post-collisional Delamination

[21] In eight models with convergence rates between 4 and 1 cm/a and mantle activation volumes of $11 \cdot 10^{-6}$ m^3/mol or higher, a second mode of delamination takes place ca. 150–200 Ma after collision, when convergence has ceased (Figure 4, model 57; age of oceanic lithosphere 80 Ma, convergence rate = 1 cm/a, $V_A = 12 \cdot 10^{-6}$ m^3/mol). Initial subduction is comparatively shallow with the slab dipping ca. 20°. After oceanic subduction and the onset of collision, net convergence of both plates continues with further descent of the subducting plate into the subduction zone. The slab sinks along the contact with the overriding plate (strong coupling), without widening of the subduction channel or trench retreat (Figures 4a and 4b). The slab does not penetrate through the 670 km phase boundary, and it rolls slightly forward instead of rolling back. The subducting continental crust (upper crust, then lower crust) separates from the lithospheric mantle at about 200 km depth, enters a return flow along the subduction channel (Figure 4b), and is added to the lower and middle levels of the orogenic plateau building on top of the subducting plate (Figures 4c and 4d). The subduction channel does not come into contact with asthenosphere. Partial melting in mid-crustal levels of the orogeny, where temperatures rise above 670°C, is observed 70–90 Ma after collision (Figure 4c, at 113 Ma model time), and expands to a ca. 200 km wide, 45 km deep area after further 30 Ma (Figure 4d, at 145 Ma model time). The partially molten continental crust moves at a peak rate of ca. 0.3 cm/a toward the foreland (i.e., away from the subduction zone toward the left). Thermal relaxation leads to elevated temperatures in the lithosphere below the partially molten crust (Figures 4c and 4d). Ca. 100 Ma after the onset of collision (which starts at 44 Ma in model 57), and 50 Ma after the onset of partial melting, the effective viscosity in the lithospheric mantle below the zone of partial melting is thermally reduced by two orders of magnitude, and necking commences. Viscous necking takes ca. 35 Ma to complete, and is accompanied by break-off of the slab along the subduction channel. The broken slab then sinks into the mantle (Figures 4e and 4f). Asthenosphere flows into the window that opens through the lithosphere of the subducting plate behind the separated slab (Figure 4f). After reaching a window width of ca. 100 km (Figure 4f), the asthenospheric flow beneath the orogen becomes divergent and splits into a clockwise flow pattern including the detaching slab at the subduction zone, and an anti-clockwise cell on the far side (with respect to the subduction zone). The lithospheric mantle on the far side of the window gets incorporated into

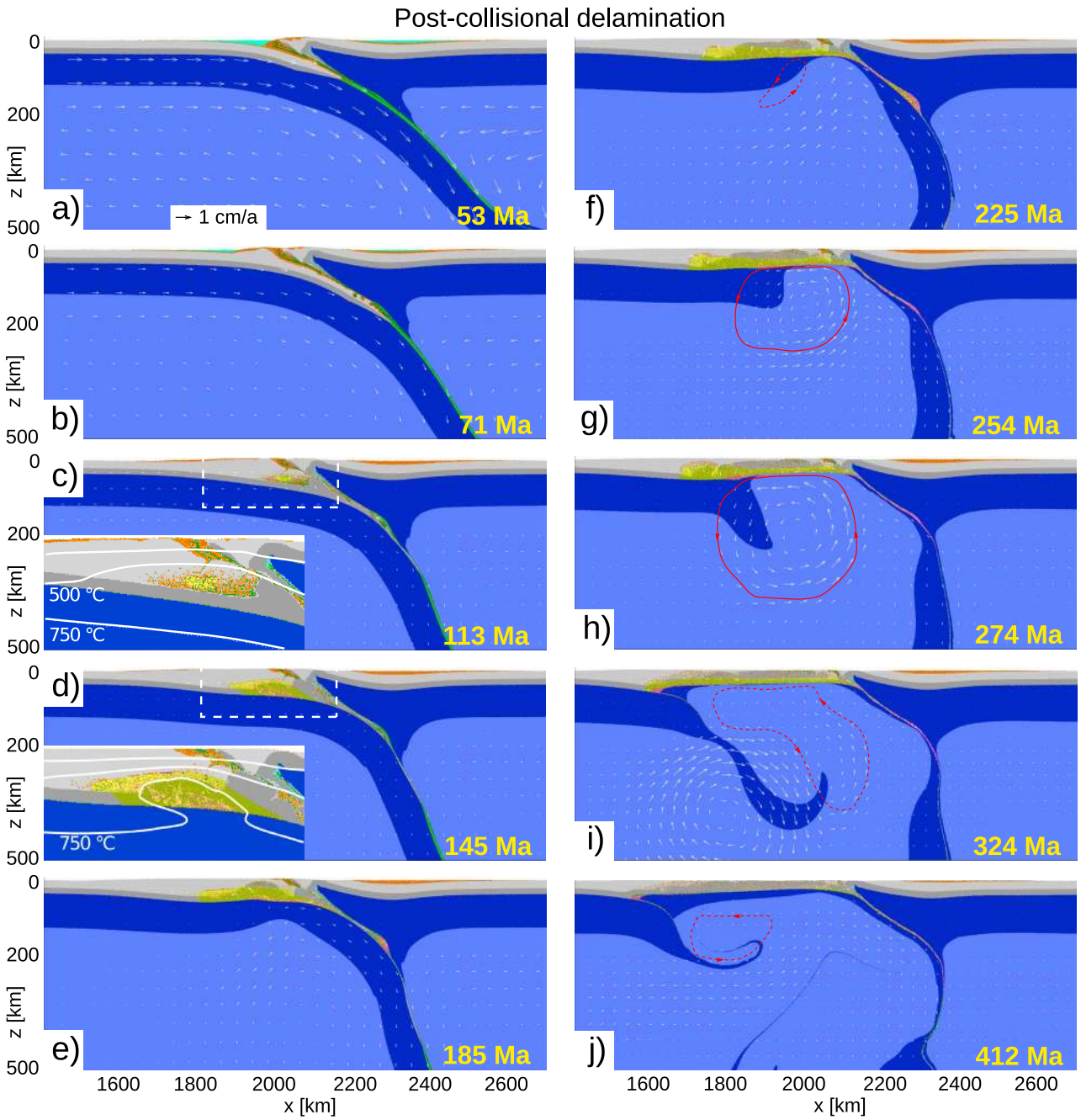

Figure 4. Post-collisional delamination within a wide and hot orogen (model 57). (a) Shallow subduction develops under slow convergence and with higher creep activation volume. (b, c) The orogen widens while convergence continues; thickening of radiogenic crust leads to partial melting in the lower crust (Figure 4c) that gradually affects larger portions of the orogen (Figure 4d). (d) A thermal anomaly develops in both crust and lithospheric mantle as illustrated by the 1023 K (750°C) isotherm. (e) The lateral difference in temperature along the lithospheric mantle induces a viscosity variation (reduction) and localizes necking below partially molten crust. (f) Crust subsequently migrates away from the suture, while the crust-free slab detaches. (g) Basal spreading of uprising asthenosphere is accompanied by lateral displacement and thickening of the lithospheric mantle at the distal side of the asthenospheric window, with mechanical decoupling between weak molten crust and lithospheric mantle. (h) Foundering of the thickened end and further uprise of asthenosphere establish a mantle flow pattern in which a new slab develops and delaminates from the crust. (i, j) Delamination propagates but is inhibited by an antithetic mantle flow pattern. Red line: approximate flow pattern that includes delamination.

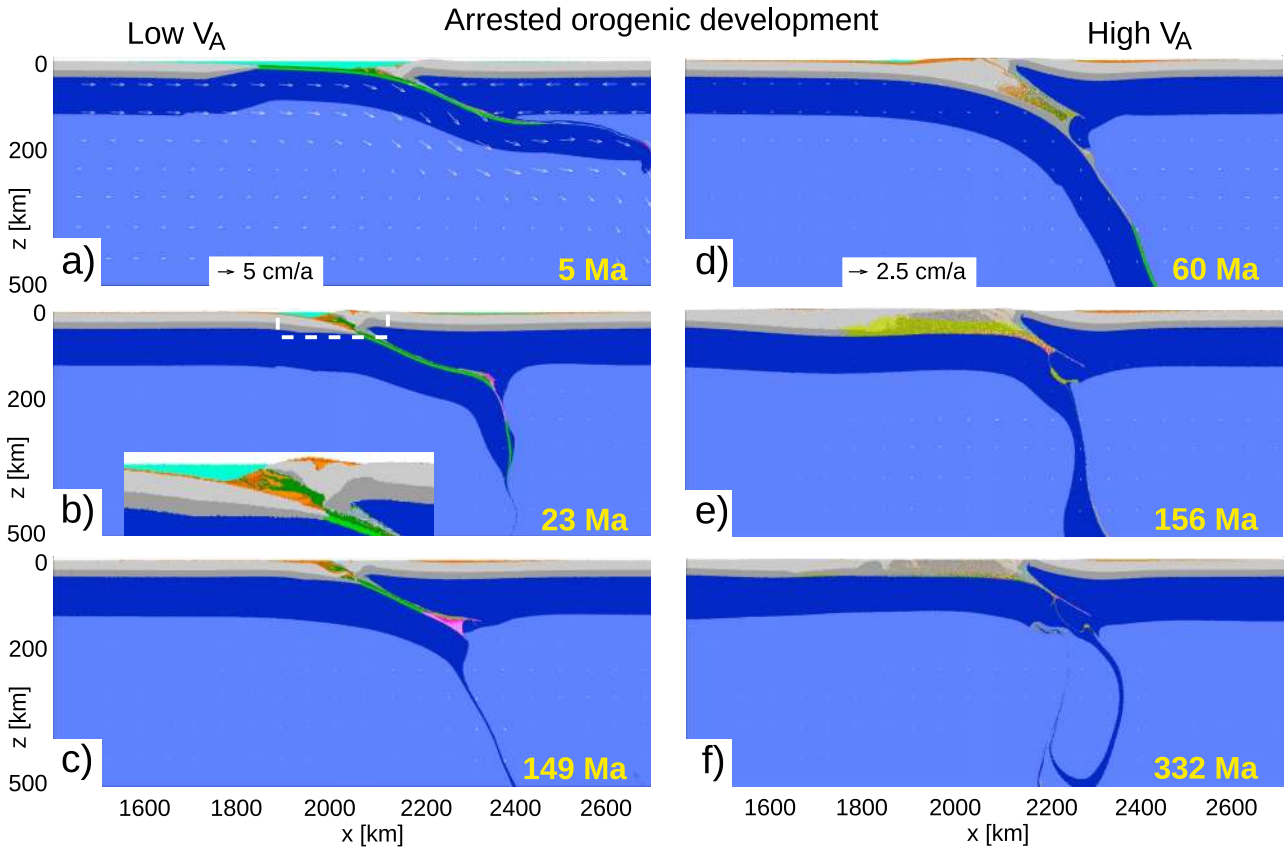

Figure 5. Non-delaminating models and arrested development. (a–c) Model 15, development of model with young and light oceanic lithosphere, similar to syn-collisional mode. Initial subduction is shallow and underthrusts the orogen (Figure 5a). After closure, the thin oceanic lithosphere provides little pull for further subduction of continental crust; convergence stagnates (Figure 5b). The thin slab breaks off easily (before and after Figure 5b), leaving little lithospheric topography below the orogen (Figure 5c). (d–f) model 52, case similar to post-collisional delamination. Thickening (Figure 5d) and partial melting (Figure 5e) as in delamination case. The detachment does not occur below the zone of partial melting, but at depth (Figure 5f). No asthenospheric window opens.

the anti-clockwise cell, is displaced away from the window and then downward, resulting in a retreat movement of a new foundering slab (Figure 4g). Self-sustaining sub-crustal subduction leads to delamination propagating along the crust-lithospheric mantle boundary (Figure 4h). Break-off of the new subducting slab leads to a reversal of flow patterns and slows down the delamination propagation (Figure 4i).

[22] In the reference model 57, collision occurs at ca. 44 Ma. Slow convergence continues until ca. 100 Ma and fades gradually. Partial melting takes place in the orogen from 113 Ma on (Figure 4c). Thermal weakening of the lithospheric mantle below the central zone of partial crustal melting amounts to one order of magnitude in effective viscosity at 145 Ma (Figure 4d), with necking beginning at ca. 165 Ma. The asthenosphere reaches the base of the orogenic crust within the window (laterally widening neck) through lithospheric mantle at ca. 215 Ma, and delamination starts to propagate along the subducting plate from ca. 250 Ma on. The initial propagation velocity is ca. 0.6 cm/a, and slows down below 0.1 cm/a at around 300 Ma. Build-up of new lithospheric mantle by cooling starts at ca. 330 Ma; the new lithospheric mantle is predicted to reach half of the initial thickness as late as ca. 460 Ma (ca. 200 Ma after the initiation of delamination).

4.3. Arrested Orogenic Development (No Delamination)

[23] Twenty-nine models with convergence rates of 1 to 5 cm/a, activation volumes between 8 and 12 $\cdot 10^{-6}$ m^3/mol, and oceanic lithosphere ranging between 20 and 100 Ma in age (the respective younger models for given other parameters), do not undergo removal of lithospheric mantle by delamination while their evolution path is variable. Of these models, those with low V_A, close to $8 \cdot 10^{-6}$ m^3/mol, develop oceanic slabs that underthrust the overriding plate shallowly (e.g., Figures 5a–5c, model 15; age of oceanic lithosphere 60 Ma, convergence rate 5 cm/a, $V_A = 8 \cdot 10^{-6}$ m^3/mol). Subsequently, only a limited frontal portion of the slab steepens (Figure 5b). Retreat of the slab is limited by slab break-off. Subduction is not self-sustaining after the onset of continental collision, and the continental crust of the subducting plate is not subducted. Owing to the limited convergence crust subducts not deeper than 60 km (Figures 5b and 5c). An elevated deformation zone of ca. 100 km width (Figure 5b) incorporates accreted sediments,

but there is almost no crustal thickening (which we define as necessary condition for an orogen) in the subducting plate. The decay of elevation is due to gradual isostatic compensation and erosional thinning, but leaves a keel of lithospheric mantle underneath the peneplaned deformation zone (Figure 5c). No partial melting of the orogenic continental crust is obtained in any low-activation volume models that do not delaminate (Figures 5a–5c). There is no exhumation of high-grade rocks, and no post-collisional extension occurs.

[24] Models with higher activation volumes ($>10 \cdot 10^{-6}$ m^3/mol), not leading to delamination (e.g., Figures 5d–5f, model 52; age of oceanic lithosphere 80 Ma, convergence rate 2.5 cm/a, $V_A = 11 \cdot 10^{-6}$ m^3/mol), resemble post-collisional delamination models for their initial evolution. Convergence ceases gradually after continental collision, with limited subduction of continental crust that enters a return flow in the subduction channel. Thickening and partial melting of continental crust takes place in a wide orogen on the subducting plate, and thermal weakening of the underlying lithosphere is observable. However, necking of the lithospheric mantle of the subducting plate does not take place below the molten orogenic crust. It occurs notably further down the slab at depths below 200 km. Consequently, no gap in the lithospheric mantle opens through which crust would be in contact with an uprising asthenosphere. In contrast to arrested models resembling syn-collisional delamination, these non-delaminating cases undergo significant partial melting of continental crust and post-collisional extension. They may expose high-grade rocks in a rather narrow area.

4.4. Transitional Models

[25] Critical parameter values differentiate between delaminating models and stable models (Figure 6). Five models, whose parameter values correspond to inferred criticality, showed incipient or short-lived, non-propagating delamination of limited (few tens of km) width (models 49, 51, 62, 70, 74, shown in Figure 6 with different symbols depending on whether asthenosphere reached the base of the crust). Although the transition has not been investigated in detail, it is likely that the transition between modes is somewhat gradual.

[26] In addition, model 81, with parameters close to criticality (convergence rate 5 cm/a, ocean age 60 Ma, activation volume $8 \cdot 10^{-6}$ m^3/mol), a thinner lithospheric mantle for the subducting plate (100 km), and a thicker lithospheric mantle for the overriding continent (150 km), showed a different transitional behavior that deserves a detailed description. Initial stages follow the evolution path of "arrested development," but stagnation of movements is temporary, and delamination propagates once initiated (Figure 7). Due to its resemblance to both "arrested development" (cf. Figure 5) and "syn-collisional delamination" (cf. Figure 2), this evolution path is regarded as mixed mode and further referred to as "transitional stagnation." Initial shallow underthrusting of the subducting plate, steepening of its oceanic slab after the onset of continental collision, and slab break-off (Figure 7a) correspond to the arrested development. The remaining slab however starts to retreat (Figure 7b), leading to a gradual separation along the contact between the two lithospheres (Figures 7c–7e) and further break-offs. Retreat is accompanied by further descent of the subducting plate into the subduction zone (Figures 7c and 7d). Subduction of continental crust to ca. 200 km depth initiates a low-viscosity return flow in the subduction channel (Figures 7e and 7f), involving partial melting of the subducted oceanic crust. Slab roll-back widens the subduction channel and facilitates its intrusion by asthenosphere (Figures 7f and 7g), in the same manner as with syn-collisional delamination.

4.5. Sensitivity Analysis

[27] The orogenic modes described above fall into parameter ranges that can be separated by approximated boundary lines (Figure 6). For given convergence rates, a critical age (thickness) of the oceanic lithosphere should exist, below which no delamination occurs (Figures 6a and 6b). Conversely, a critical convergence rate value should exist for given ocean ages. Modeled without melting, the boundary line in age - convergence space is inclined and delamination initiation depends on both parameters (Figure 6a). If melting is implemented, the boundary becomes nearly parallel to the convergence rate axis, indicating that the convergence rate has little influence on delamination initiation (Figure 6b). In the more realistic models with melting, a critical oceanic age of ca. 60 Ma, corresponding to a 65 km thick oceanic lithospheric mantle, needs to be exceeded to initiate delamination. The effect of oceanic age on delamination propagation is shown in Figure 8a, where models with melting (thick lines) delaminate slightly faster and further than those without (thin lines). Oceanic ages of 60 Ma, close to criticality, show slower delamination rates (ca. 0.4 cm/a) that are sensitive to slab break-offs (change in slope in Figure 8a, red line), while older oceans delaminate faster (ca. 1 cm/a) and are less sensitive to break-offs.

[28] An activation volume $V_A >$ ca. $10 \cdot 10^{-6}$ m^3/mol (exemplified by reference model 57, Figure 4) leads phenomenologically to the following changes compared to values of ca. $8 \cdot 10^{-6}$ m^3/mol (e.g., Figure 2, reference model 18, which additionally has a different oceanic age): a) a shallower initial subduction; b) reduced retreat after collision; c) the build-up of wide orogens with shallowly inclined lithospheric mantle; d) the possibility of post-collisional delamination. The evolution diagram in V_A - oceanic age space (Figure 6c) shows that an increasing V_A disfavors syn-collisional delamination, in accord with shallower subduction and less effective roll-back. Increasing V_A corresponds to increasing viscous "resistance" to free slab movements and likely to the incitement of convective flow. Increasingly older oceanic slabs, hence resultant stresses (slab pull), are needed to start this mode of delamination.

[29] Figure 6d demonstrates that the mode of orogenic evolution strongly depends on V_A. Syn-collisional delamination is limited to V_A values $<10.5 \cdot 10^{-6}$ m^3/mol, whereas post-collisional delamination is only possible above $11 \cdot 10^{-6}$ m^3/mol for the given age. Arguably, both delamination mechanisms are separated by a parameter range corresponding to arrested development, and the distinction between arrested development and post-collisional delamination modes is insufficiently explored. Although the correlation of post-collisional delamination with shallow subduction and wide orogens is evident, it is not restricted to very slow convergence zones.

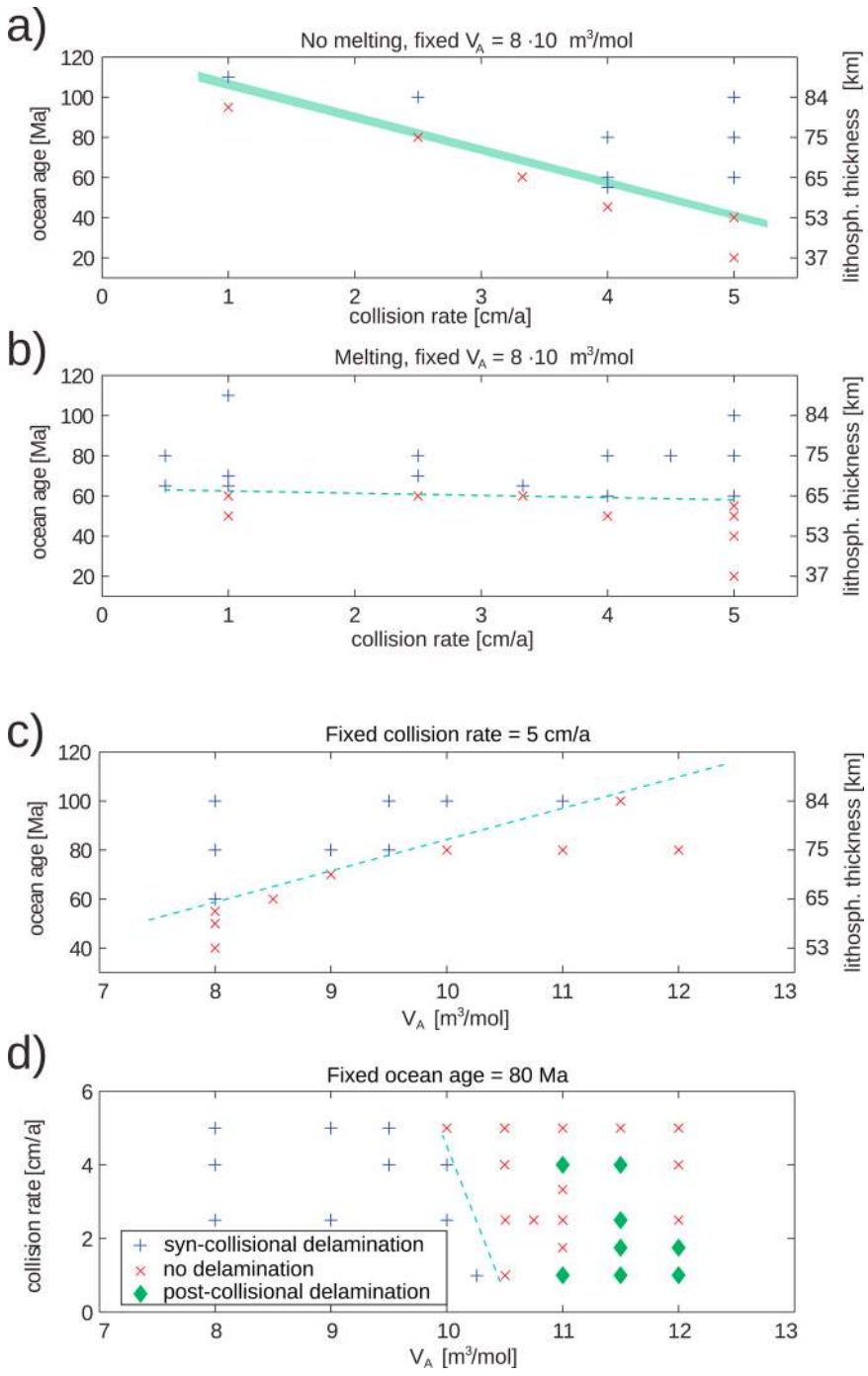

Figure 6. Model evolution diagrams. Figures 6a and 6b show diagrams in oceanic age - convergence rate space for otherwise fixed parameters. (a) Melting suppressed. Weakening of the plate interface is likely contingent on shear heating. (b) In the presence of competing weakening mechanisms (partial melting and possible return flow in the subduction channel), no cross-correlation of outcome exists between age and convergence rate. The model in Figure 6a below the inferred boundary line has been re-run with the same result. Figures 6c and 6d show model evolution diagrams with reference to creep activation volume parameter for mantle. (c) In V_A -age space, at fixed convergence rate; (d) in V_A – convergence rate space at fixed oceanic age. In Figure 6c, increasing activation volumes require increasing age (available thickness) for delamination development. In Figure 6d, slower convergence extends the range in which syn-collisional delamination is possible toward higher V_A values. High V_A values are not compatible with syn-collisional delamination, but lead to an accumulation of thickened crust that facilitates post-collisional delamination in front of the suture.

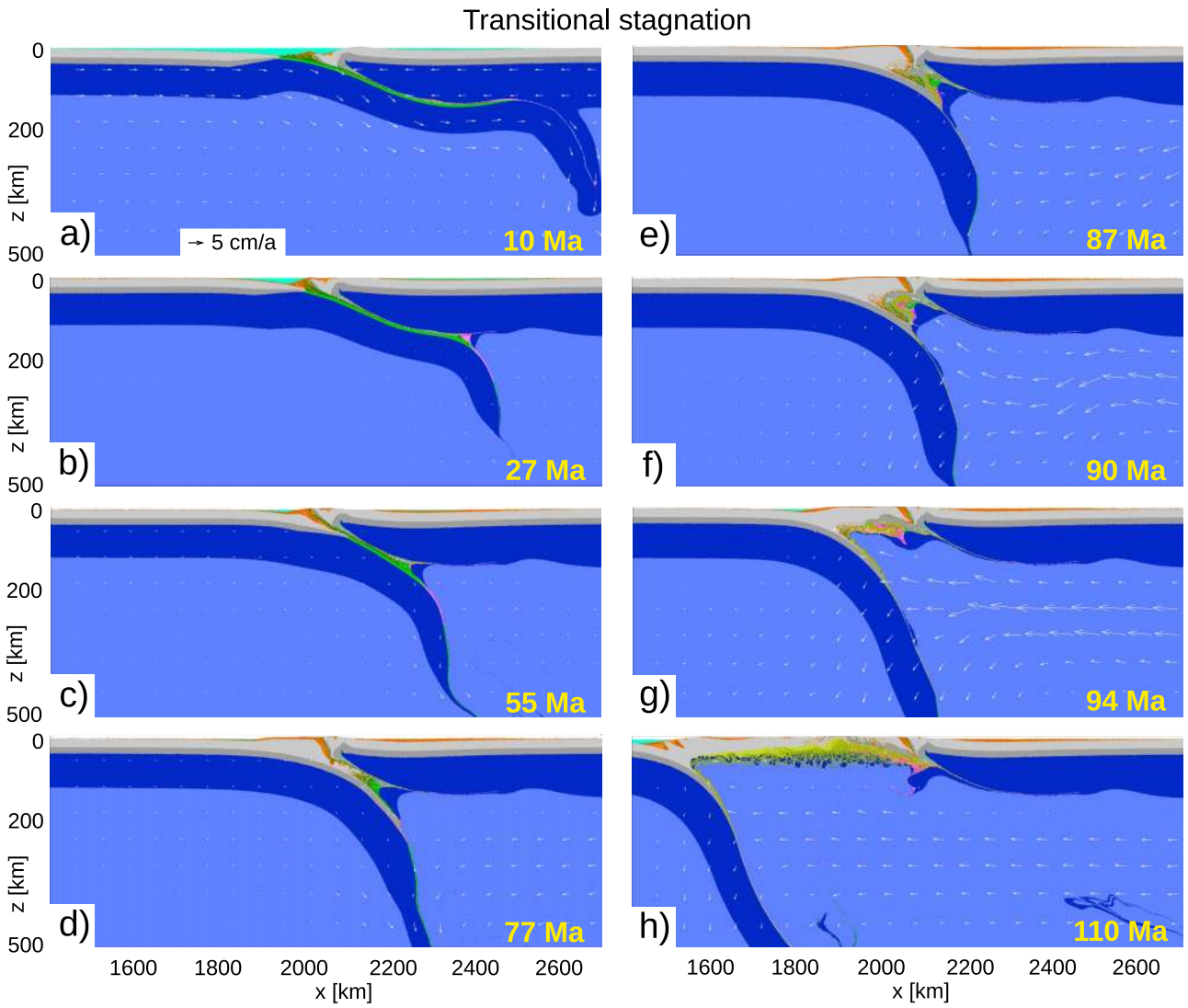

Figure 7. Transitional stagnation of development and delayed delamination (model 81). A collision zone initially exhibits an evolution similar to models that do not undergo delamination (cf. Figure 5). (a) After shallow underthrusting subduction, the onset of collision slows down plate motions (Figure 7b). (b, c) Melting of oceanic crust along the plate contact however later enables decoupling. (d, e) Retreat of the coherent slab, and (f–h) opening of a sub-crustal asthenospheric window alter the evolution to a case similar to syn-collisional delamination. The initial geometry resembles cases of post-collisional delamination, while the delamination process resembles syn-collisional delamination.

[30] Studies of other parameters are limited and the investigation of their effect is qualitative. A thicker overriding lithosphere requires the subducting plate to be underthrust to larger depths. This effect, possibly together with a slight increase in coupling due to a longer plate contact, is sufficient to alter the evolution path of a close-to-criticality syn-collisional delamination model and to generate the mixed mode of "transient stagnation" as described with model 81 (Figure 7).

[31] Higher erosion rates of 3 mm/a (model 78) lead to stronger crustal thinning and deeper exhumation, but has a minor effect on delamination (Figure 8d). Lowering the sedimentation rates by three and six orders of magnitude (models 79, 80, respectively) yields smaller amounts of hydrated sediments ingested into the subduction zone and hampers delamination (Figure 8d, with propagation rates as slow as 0.4 cm/a). Adapting a felsic granulite rheology [*Ranalli*, 1995] for the lower crust leads to rapid syn-collisional delamination of more coherent crust (Figure 9; model 83) with a delamination rate of ca. 5 cm/a, 5× higher than in the reference case (Figure 2; model 18).

5. Discussion

[32] Delamination modes differ in timing, location and conditions of initiation, but have in common a lateral propagation of delamination along the subducting plate. Mechanisms similar to incipient syn-collisional delamination have been observed in numerical studies [*Gerya et al.*, 2008; *Warren et al.*, 2008; *Faccenda et al.*, 2009; *Duretz*

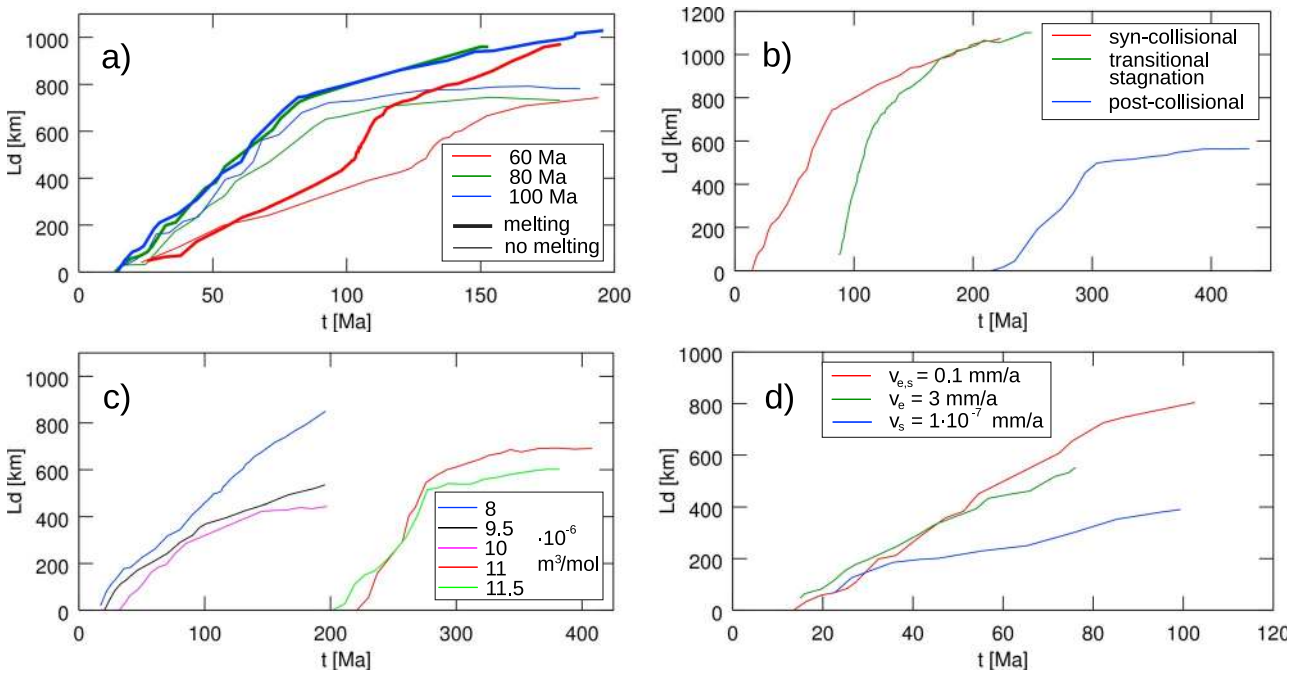

Figure 8. Delamination width Ld (horizontal gap width measured at the depth of the delamination point) over time as function of different parameters. (a) Syn-collisional delamination models) with different oceanic ages. Thin lines denote models where melting is disabled (models 11–13), thick lines models with melting (default; models 16–18). Melting enhances delamination dynamics. (b) Different evolution modes: red – syn-collisional delamination (model 18, Figure 2), green – transitional stagnation (model 81, Figure 7), blue – post-collisional delamination (model 57, Figure 4). (c) Variation of activation volume in otherwise identical models (models 19, 50, 54, 55, 63). (d) Variation of surface processes: red – standard values (model 17), green – erosion rate (v_e) increased by a factor of 30 (model 78), blue – sedimentation rate v_s reduced by a factor of 10^6 (model 79). Scarcity of hydrated sediments that enter the subduction zone has a negative effect on delamination.

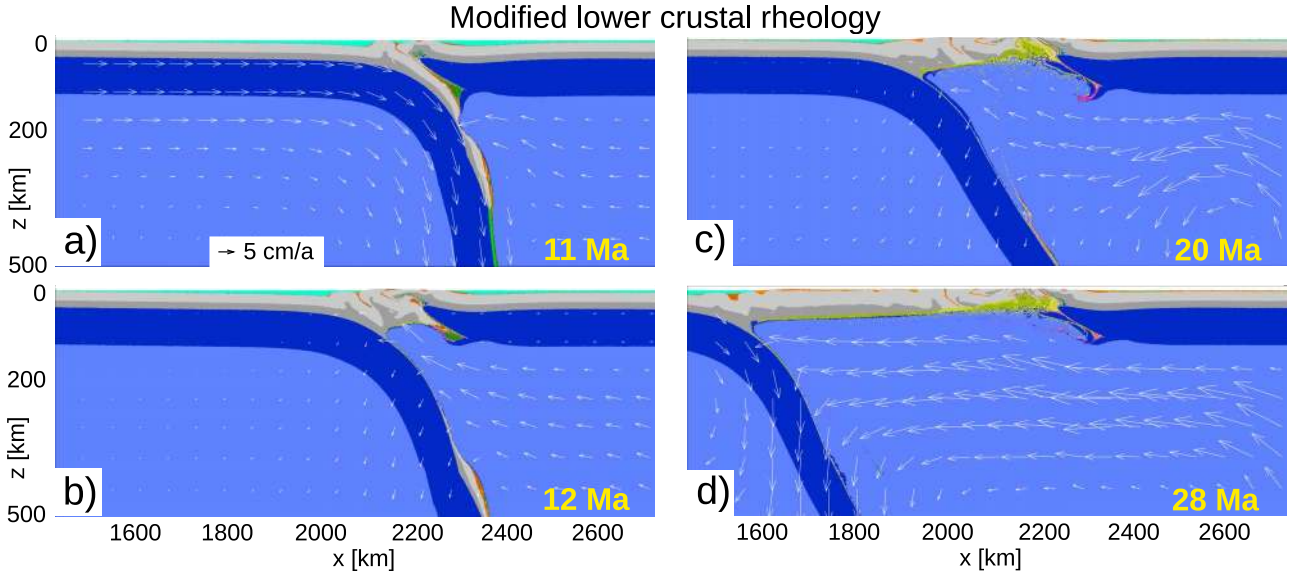

Figure 9. Effect of lower crustal rheology. Felsic granulite rheology [*Ranalli*, 1995] leads to rapid (ca. 5× faster) delamination, widening of the asthenospheric window which propagates faster than partial melting of the exposed crust, and localized crustal thickening (model 83).

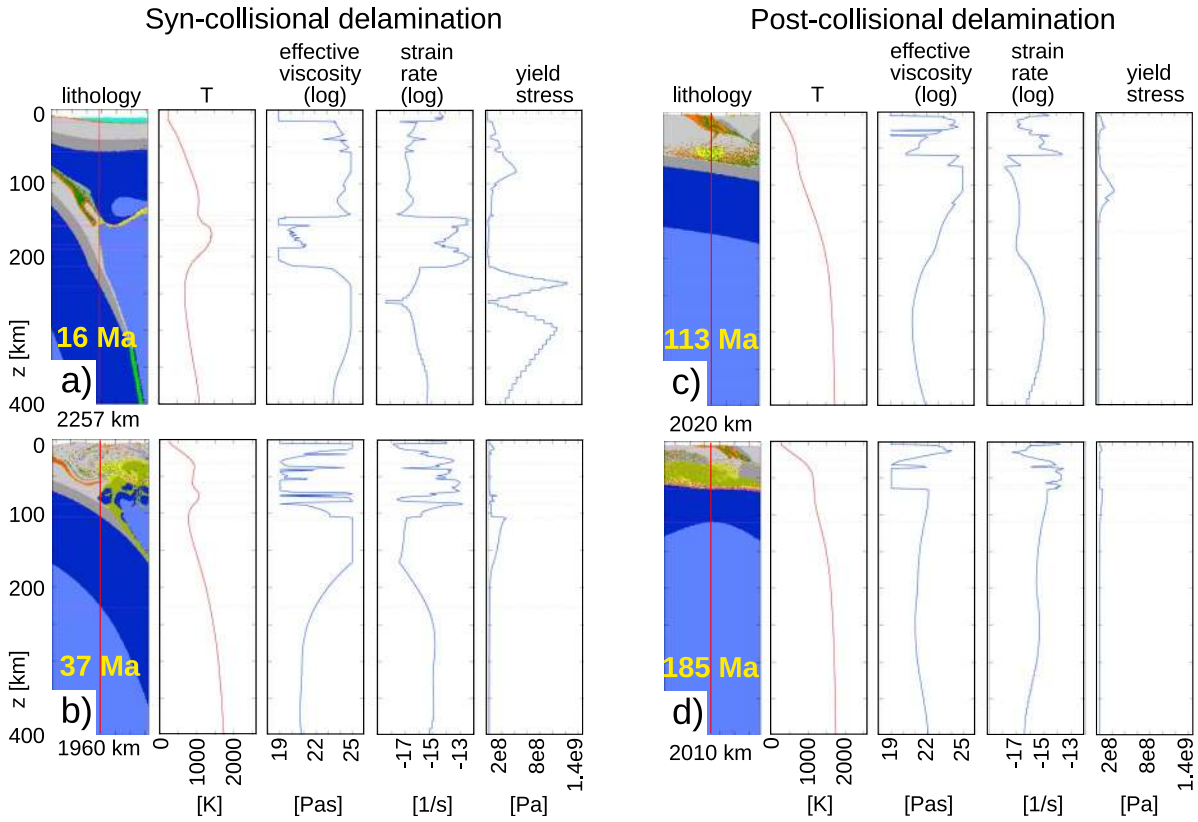

Figure 10. Initiation of delamination for reference cases. (a, b) Syn-collisional delamination (model 18). Elevated temperatures correspond to low effective viscosity, and preferred partitioning of strain into these levels. Note disappearance of undisturbed rheological strength profile from Figure 10a to Figure 10b. (c, d) post-collisional delamination (model 57). Heating from the top decreases the strength of the lithospheric mantle.

et al., 2011] and scaled analogue experiments [*Boutelier et al.*, 2004; *Göğüs et al.*, 2011]. *Faccenda et al.* [2009] emphasized the importance of mobile volatile phases for decoupling along the subduction zone, producing precursors of transitional arrest and syn-collisional delamination. *Duretz et al.* [2011] modeled deep slab break-off preceding the opening of an asthenospheric window into the lithospheric mantle of the subducting plate, with the same parameters that produce syn-collisional delamination on a larger time-scale.

[33] Post-collisional delamination is phenomenologically similar to tensile and ductile detachment models presented by *Sacks and Secor* [1990]. These models called however for syn-convergent detachments that would open small asthenospheric windows into the lithospheric mantle and would not initiate propagating, long-lived delamination. Our post-collisional delamination mode is a novel mechanism that can be used to describe removal of lithospheric mantle and high-grade metamorphism as late as 200 Ma after collision.

[34] The observation of one model (model 81; Figure 7) with transitional stagnation, in which delamination initiates ca. 70 Ma after collision, suggests that delamination is feasible over an extended time range after collision. This would provide an important alternative mechanism of lithospheric removal by (planar) delamination *sensu stricto* instead of viscous dripping (convective removal) in settings considered to be anorogenic (see converging trajectory in Figure 8b). Our new mode(s) would allow for resumed post-collisional sub-crustal subduction and propagation of mantle removal.

5.1. Initiation, Propagation, and Termination

[35] In the initial sub-collisional delamination phase of the most deeply subducted continental crust (Figure 2c), heating from the asthenosphere reduces strengths, and the locus of viscous delamination under low yield stress lies accordingly within the crust (Figure 10a). With delamination propagating sub-horizontally, the separation occurs at the base of the upper continental crust, where the lateral proximity of the intruding asthenospheric wedge is sufficient to elevate temperatures over 1000 K and thus reduce effective viscosity (Figure 10b).

[36] Post-collisional delamination below thickened continental crust initiates while relative plate movements are negligible (Figures 4f, 4g, and 11c). After thermal relaxation and tens of Ma of post-collisional maturation, the rheologically weakest part is not the subduction channel, but the partially molten horizontal flow channel at the base of the orogen (Figure 10d).

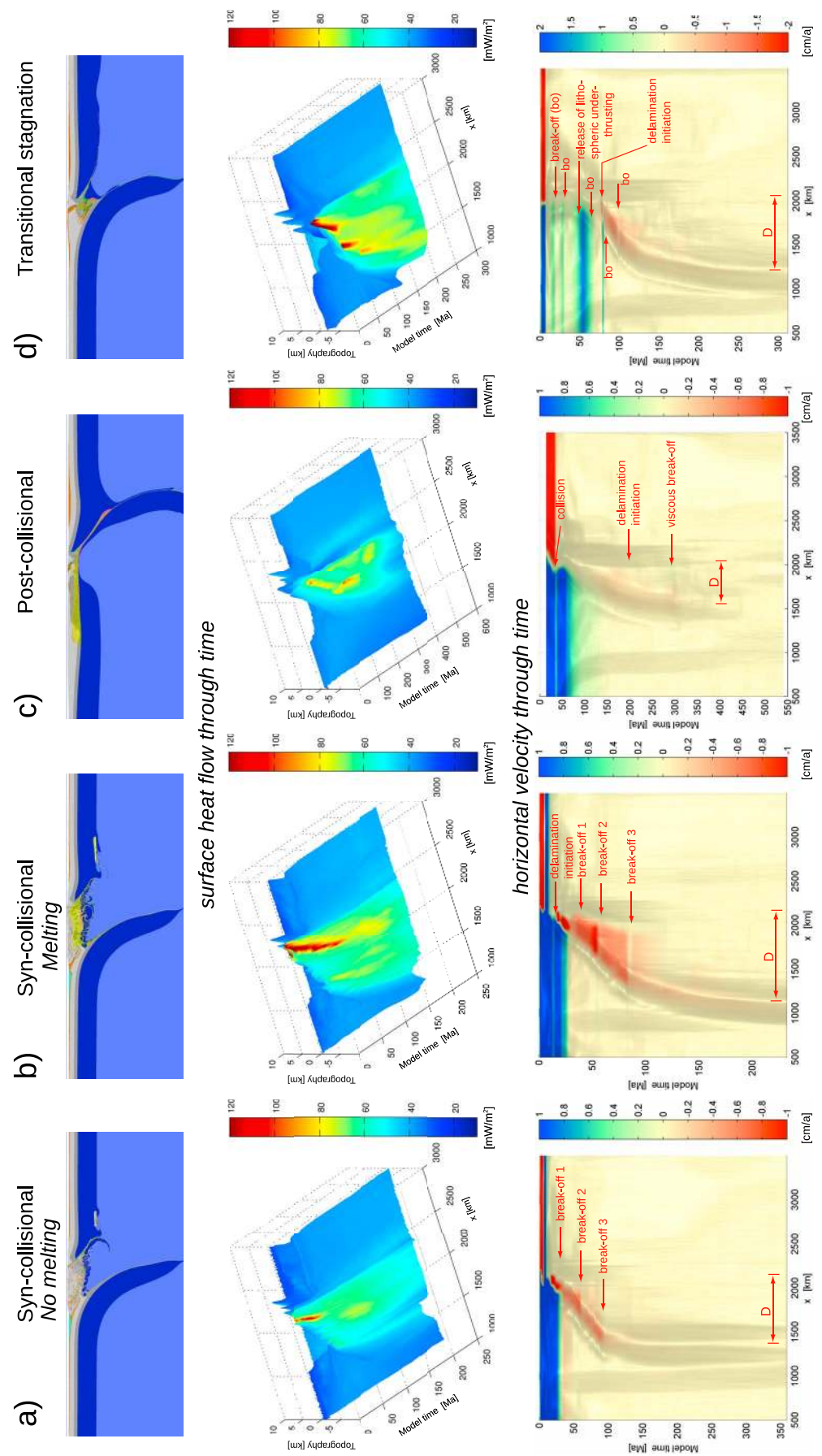

Figure 11. Comparison of surface expressions between different delamination modes. (a, b) syn-collisional delamination without (model 11) and with melting (model 18), (c) post-collisional delamination (57), (d) transitional case with initial arrest (model 81). Uppermost row: exemplary lithological field, middle row: surface heat flows, bottom row: horizontal near-surface velocities. Topographic evolution and heat anomaly are in qualitatively agreement. The incorporation of melting in otherwise identical models (Figures 11a and 11b) increases surface heat flow. Horizontal velocities show that after collision, movements in the overriding continent first come to a halt. However, after the onset of delamination, the thickened orogenic crust above the asthenospheric window starts to extend and to move toward the subducting plate. The complex break-off history in the transient model (cf. Figure 7) is reflected in the surface kinematics. D: width of delaminated domain.

[37] In absence of an active subduction channel, no plate-scale weak zone is available to allow local decoupling between lithospheric mantle and continental crust, vertical movement of lithospheric mantle, and nucleation of delamination as in the syn-collisional case. While the partially molten orogenic crust provides a rheological strength minimum that extends for hundreds of km horizontally, the geometry of decoupling only allows for differential, horizontal large-scale movements between crust and coherent lithospheric mantle, precluding vertical movements (foundering) and a connection with the asthenosphere. Horizontal movements of the lithospheric mantle are hampered by its lateral (viscous) stiffness and its pinning in the collisionally congested subduction zone. Without means to "cut across" the lithospheric mantle, the same meta-stability is maintained as in non-orogenic continental plates. Eventually, necking of the mantle lithosphere allows a localized separation, the mobilization and release of lithospheric slabs into the subduction zone, the formation of a conduit through the lithospheric mantle, and the connection with hot asthenosphere. Necking takes place only after the strength in the lithospheric mantle is reduced (Figure 10d), by high temperatures gradually increased from above by the partially molten crust (Figures 4c and 4d), whereas the tensile stresses are provided by the leveraged weight of the inclined slab [cf. *Sacks and Secor*, 1990; *Duretz et al.*, 2011; *Wallner and Schmeling*, 2011]. While the upwards flow of asthenosphere is driven by slab detachment and mass balancing, its convective organization may be influenced (Figure 4g) by a small-scale edge-driven convection component [*King and Anderson*, 1998]. Post-collisional delamination models describe orogens that are wide and hot after a period of tectonic quiescence, depending directly on the thermal maturation of the orogen and the rise of temperatures in its interior.

[38] Sensitivity analyses show that the influence of convergence rate on the subsequent occurrence of delamination (for fixed activation volumes and oceanic ages) is strongly reduced if melting is modeled (Figures 6a and 6b). The rate dependency with suppressed melting corresponds to weakening of plate coupling due to shear heating [*Faccenda et al.*, 2009], while weakening and decoupling can be accomplished more efficiently (and independent of rate) with partially molten rocks in the subduction channel. Both syn-collisional delamination (Figure 2) and delamination after transitional stagnation (Figure 7) initiate after deep subduction of continental crust and its exposure to the asthenosphere. The quickly developing return flow distributes partially molten low-viscosity rocks within the subduction channel, reducing the coupling strength along the plate interface. The self-consistently developing subduction channel creates a low-viscosity conduit across the lithospheric mantle; such a conduit had to be imposed ad hoc in earlier numerical [*Bird*, 1979; *Schott and Schmeling*, 1998; *Göğüs and Pysklywec*, 2008b; *Valera et al.*, 2008, 2011; *Wallner and Schmeling*, 2010, 2011] and laboratory experiments [e.g., *Göğüs et al.*, 2011; *Bajolet et al.*, 2012].

[39] The development of either syn-collisional or post-collisional delamination (Figures 6d and 8c) exhibits a first-order dependence on the viscous rheology parameter V_A, which has been used as the control parameter for the viscous rheology for mantle rocks. This general sensitivity of delamination to viscosity parameters is comparable to that of previous studies [*Schott and Schmeling*, 1998; *Morency and Doin*, 2004; *Valera et al.*, 2011; *Gray and Pysklywec*, 2012].

[40] The continuation of delamination or slab subduction after break-offs is a common observation (Figures 3 and 12). Foundering slabs initiate upper mantle convective flow that encompasses subduction and delamination and follows roll-back movements.

[41] Convective flow continues despite slab break-off, exerting viscous suction on the new slab tip. Convective suction leads to further subduction, even if direct slab pull is temporarily reduced [cf. *Bird*, 1979; *Guillaume et al.*, 2010; *Valera et al.*, 2011]. Indirect, inert convective transmission of the pull of detached slabs that sink into the mantle stabilizes subduction [*Conrad and Lithgow-Bertelloni*, 2002], roll-back trench retreat, and propagation of delamination.

[42] The initial propagation rates of delamination, ca. 0.6 and 1 cm/a for the major reference cases, are in the low range compared to those obtained by *Bird and Baumgardner* [1981] (0.3–8 cm/a, while using slab velocities up to 32 cm/a), and by *Morency and Doin* [2004] (0.2–10 cm/a). We have punctually obtained rates up to 5 cm/a only for two exploratory models (models 82, 83) with different lower crustal rheology, however without coverage of the parameter space around these models. This is consistent with the notion that lower crustal rheology exerts a major control on the development of delamination [*Schott and Schmeling*, 1998; *Morency and Doin*, 2004]. In contrast, delamination speeds in *Göğüs and Pysklywec* [2008b] exceed 20 cm/a for the first 700 km of asthenospheric window width. *Gray and Pysklywec* [2012] produced delamination rates of ca. 3–4 cm/a under constant convergence; compared with our rates, this may indicate a sensitivity of delamination propagation to external kinematic conditions.

[43] *Bird and Baumgardner* [1981] have noted that once delamination goes on, terminating it becomes a fundamental problem. This could be either accomplished by complete consumption of the delaminating continent or by slab break-off. Our results suggest that break-off is not necessarily terminating propagation. Plots of total delamination versus time (Figure 8) indicate however that propagation generally slows down after delamination of ca. 550 to 750 km of continental lithosphere. This agrees with the fact that most mantle convection patterns are roughly limited to the upper 670 km of mantle (the phase transition being possibly depressed by accumulated slab material) (Figure 3 and 12). We propose that delamination is an inseparable part of mantle convection, that convection cells are vertically limited to the spinel-perovskite transition and become inefficient when the lateral size exceeds the vertical limit, and that propagation of delamination beyond ca. 700 km, albeit being possible and observed, is less favorable.

5.2. Orogenic Characteristics and Geological Exposure

[44] The three orogenic characteristics (i) crustal thickening, (ii) topography, and (iii) elevated temperatures (partial melting and high-grade metamorphism) develop predominantly after delamination initiation in the syn-collisional case, reaching their maximal magnitude with the cessation of convergence ca. 20 Ma later (Figures 2 and 11b). The topographic high is narrow (<200 km) and crustal temperatures are below partial melting temperatures at the onset of

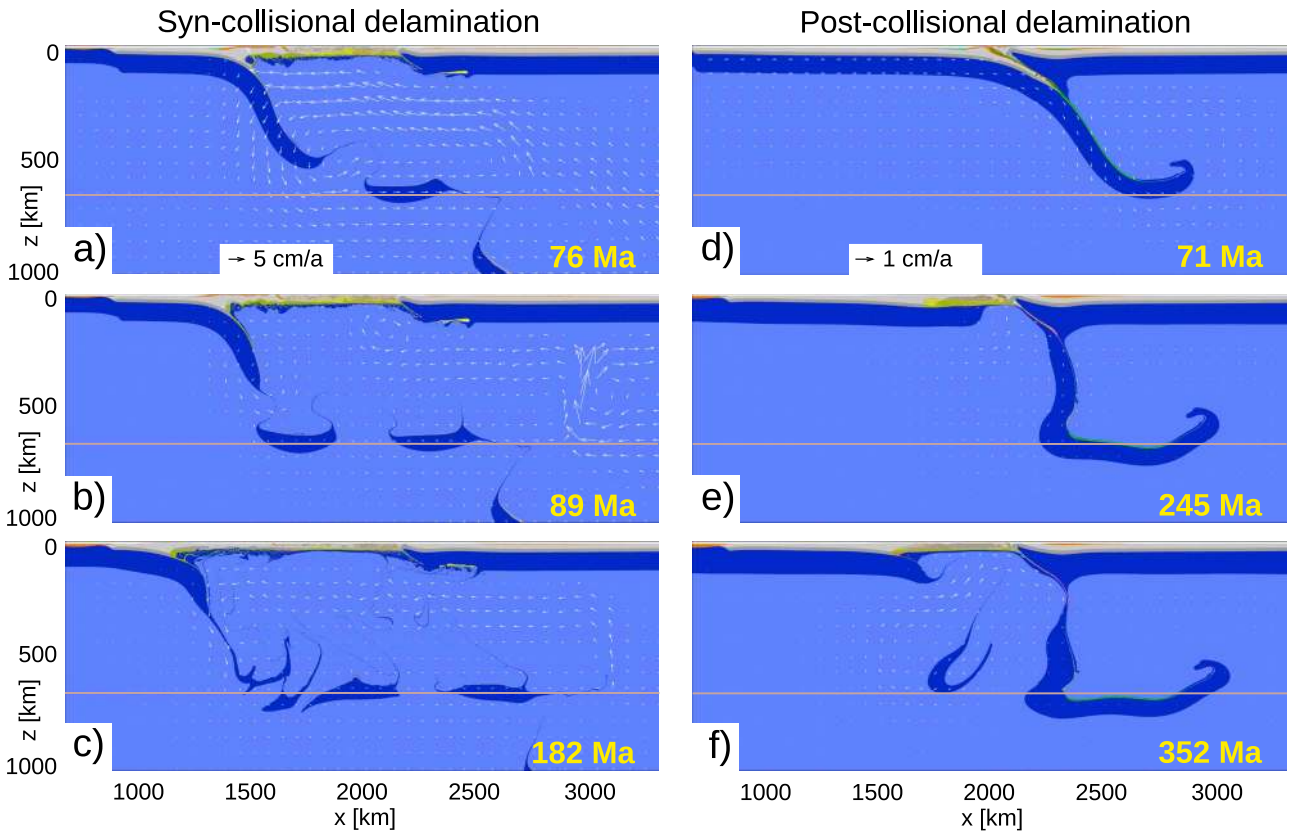

Figure 12. Large-scale dynamic effects of the phase transition in the mantle at 670 km. Discontinuity is semi-permeable (see deeper slab fragments in Figures 12a–12c), but exerts first-order control on flow patterns. (a–c) reference case for syn-collisional delamination (model 18), (d–f) for post-collisional delamination (model 57). Note forward rolling of slab tip. Grey line indicates depth level of phase transition.

delamination. Partial melting in the syn-collisional case is due to juxtaposition of continental crust with asthenosphere. The three characteristics propagate diachronously with delamination along the subducting plate, forming a sideways mobile belt (Figure 11b). The propagation of topography and transient local crustal thickening agree with previous studies [*Valera et al.*, 2008, 2011; *Göğüs and Pysklywec*, 2008b]. Given the numerical limitations in surface predictions, notably in simplifying surface processes, no surface prediction with temporal or spatial precision is presented; a range of time-resolved topography predictions obtained with different formulations is available from *Schott and Schmeling* [1998], *Göğüs and Pysklywec* [2008b], *Valera et al.* [2011], and *Gray and Pysklywec* [2012]. *Gray and Pysklywec* [2012], while prescribing constant convergence, obtained uniform plateau elevations of 5 km height over several hundreds of km, which is not observed at comparable scales in our models.

[45] In the post-collisional case, the three characteristics reach their peak prior to the onset of delamination, and subsequently diminish over the entire orogen (Figures 4 and 11c). Thickening of continental crust and the highest topography occur during collision; lateral redistribution of crust in a partially molten channel flow sets on before delamination.

[46] In the model of transitional stagnation, all characteristics develop before delamination, but reach their maxima after delamination; the further development is identical to syn-collisional delamination (Figures 7 and 11d).

[47] Delaminated, non-subducted crust overlying the asthenospheric window through lithospheric mantle shows increased crustal heat flow values (ca. 70–80 mW/m^2 on average, peak values >120 mW/m^2; Figure 11) after delamination, partial melting, and formation of a contiguous layer (channel) of partially molten material. The change from conductive to convective heat transfer underneath the crust increases the efficiency and rate of heat transport (Figure 11); small-scale convection within the crust mimics the possible effect of widespread granitoid intrusions and migmatite domes in nature [e.g., *Vanderhaeghe*, 2009]. The comparison of identical models with (model 18) and without melting (model 11) shows higher surface heat flow values (up to a factor of two) when melting is modeled (Figures 11a and 11b). The difference can be explained by a higher efficiency of heat transport if it has a component of advection, which is facilitated by a lowered viscosity of partially molten rocks, showing that melting is an important factor that must be considered.

[48] Buoyancy-driven return flow in the subduction channel brings up continental crust into the orogen that has been subducted to depths >200 km (Figures 2c and 4b), which may hold records of initial ultra-high-pressure (UHP) metamorphism after exhumation. Deep subduction of

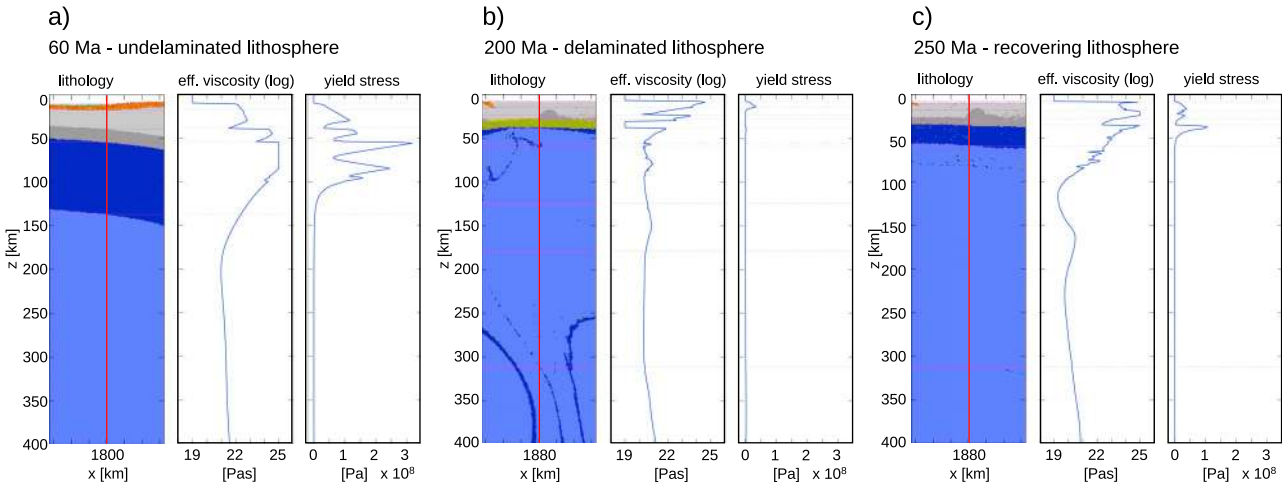

Figure 13. Rheological effect and long-term impact of delamination (model 39, syn-collisional delamination). Shown are sections with effective viscosity and yield stress for (a) undelaminated, (b) delaminated and doubly weakened, (c) partially replenished continental plate. Figure 13a shows effect of different competing deformation mechanisms on mantle lithosphere strength, e.g., the Peierls mechanism. Delamination has started at ca. 14 Ma, but the delamination propagation tip has not yet passed through in Figure 13a. The integrated strength of delaminated lithosphere (Figure 13b) is 1–2 orders of magnitude smaller than that of undelaminated lithosphere (Figure 13a). Even ca. 235 Ma after delamination, the integrated strength is lowered by ca. one order of magnitude (Figure 13c).

continental crust and subsequent exhumation are in agreement with previous models of collision zones [*Gerya et al.*, 2008; *Warren et al.*, 2008; *Valera et al.*, 2008; *Duretz et al.*, 2011]. Natural exposures of crustal UHP rocks corroborate early subduction to depths ≫100 km with subsequent rapid exhumation to shallower crustal levels, and are reported from a variety of localities, such as the Western Alps [e.g., *Chopin*, 1984], the Kazakh Kokchetav Massif [e.g., *Shatsky et al.*, 1999; *Hermann et al.*, 2001], the Variscan Belt [e.g., *Bakun-Czubarov*, 1991; *Kotkova et al.*, 2011], the Western Gneiss Region of Norway [e.g., *Lappin and Smith*, 1978], or the Dabie Shan [e.g., *Xu et al.*, 1992; *Hacker et al.*, 2000]. The highest pressure estimates of up to 4.5 GPa [*Lappin and Smith*, 1978; *Hermann et al.*, 2001] and the correlation of diamond stability and pressures of ca. 4 GPa suggest that continental crust could even undergo subduction to deeper than 150 km [cf. *Chopin*, 2003].

[49] The (not subducted) continental crust overlying the asthenospheric window undergoes basal heating and partial melting on a large area without undergoing substantial vertical displacement. The longevity of partial melting (e.g., Figures 2e–2g) implies that the most recent metamorphism recorded in eventually exhumed rocks would be HT-LP metamorphism that could significantly postdate delamination.

[50] Large-scale crustal uplift and erosion occur over the whole delaminated domain, but are strongest at the front of the propagating delamination. Early peak uplift rates over the extruding subduction channel are more than 2 cm/a while peak rates at the propagating delamination front reach ca. 0.2–0.3 cm/a. In comparison, scaled analogue models predict early peak uplift rates of up to 10 cm/a, and average rates of ca. 1 cm/a [*Boutelier et al.*, 2004].

5.3. Thermal Evolution and Implications

[51] In our reference models, the time between delamination of the subducting lithospheric mantle and renewal of a mechanically rigid lithosphere by cooling of the asthenospheric window amounts to 100–150 Ma. In the view of overall mineralogical similarity between asthenospheric and lithospheric mantle, the problem of lithospheric replenishment is simplified to a thermal problem, as mechanical differences are a function of homologous temperature. An estimate for the time needed to regain half of the initial lithospheric thickness by static, conductive cooling amounts to ca. 60 Ma [*Nelson*, 1992]. In contrast, the reconstruction of lithosphere in our models is negligible 60 Ma after delamination, and characteristic half-thickness cooling after delamination is delayed by a factor of ca. 3. Convection in the asthenospheric window implies almost constant Moho temperatures, geothermal gradients, and minor cooling in the overlying crust. Predicted heat flow reduces slowly over the delaminated domain (Figure 11).

[52] The delayed renewal of lithosphere compared to the static cooling estimate can be explained with the mantle flow that prevails in the asthenospheric window and that includes delamination and subduction (Figure 12). Sub-crustal asthenosphere that could cool to form new lithosphere is constantly replaced with new asthenosphere from depth by convection, maintaining adiabatic mantle temperatures. The thickness contrast between delaminated and undelaminated lithosphere, both having nearly isothermal bases, makes the asthenospheric window potentially susceptible to edge-

driven convection [e.g., *King and Anderson*, 1998] once the effect of slab dynamics have migrated with delamination and become locally diminished. While not systematically observed (Figures 2, 4, and 7), this rather weak convection mechanism may be intermittently operating (Figure 12b). With the degree of complexity reproduced in the numerical models, static cooling is not suited as an approximation for post-delamination cooling, and mantle flow patterns have not only a first-order importance in the propagation and cease of delamination, but also in the renewal of lithosphere.

[53] On a cautionary note it should be pointed out however that while the principally slower observed renewal of delaminated lithosphere is reasonable due to the precedence of convective over conductive heat transport, the timing might vary for various reasons that are not surveyed completely. For example, surface processes may play a role in eroding, exhuming, and cooling crust (steady vertical advection). A natural Moho and lithosphere-asthenosphere boundary may exhibit topography that may complicate delamination propagation and mantle flow; processes at other plate boundaries and within the deeper mantle may influence and reduce the stability of large-scale flow patterns in the upper mantle.

[54] The integrated strength of a delaminated plate is reduced in two ways. First, a major part of its strength is lost with the lithospheric mantle. Second, thermal relaxation after exposure to asthenosphere leads to strong heating and melt-weakening of the remaining crust. The integrated strength of the plate is reduced by 1–2 orders of magnitude, and is held entirely by the crust. Figure 13 shows in vertical profiles [cf. *Ranalli*, 1995] the loss and slow restoration of strength following delamination, which is attributed to ongoing convection and the slow restoration of lithospheric mantle. The plate strength is potentially low enough to facilitate continental break-up and rifting, as *Rey* [2001] has suggested for the convective removal of lithospheric mantle. Despite some caution, our models demonstrate that delaminated plates can remain without significant lithospheric mantle on a time-scale of 100–200 Ma.

5.4. Comparison to Geological Analogues

[55] The syn-collisional delamination mode provides the first geodynamically consistent numerical reproduction of a convergent plate boundary zone that is self-sustaining and evolves from subduction over collision to delamination and orogenic collapse. The area between unaffected subducting plate (at the trench) and unaffected overriding plate (at the initial location of subduction) reaches widths of hundreds of km (e.g., Figure 2g). This area has no lithospheric mantle and shows a transient trenchward movement of such characteristics as crustal thickening followed by crustal extension, HT/LP metamorphic conditions in the continental crust, and anatexis of the lower crust (Figures 2e–2g; Figure 11).

[56] Potential analogies are documented in the complex Mediterranean region. In the Rhodope, Cenozoic extension post-dates Late Jurassic to Early Cretaceous crustal thickening, imbrication, and subsequent extensional gravitational adjustment [*Burg*, 2012]. The later event accounts for the fault-bound exhumation of extensional metamorphic core complexes after advanced peneplanation of the metamorphic Rhodope, and is internally associated with low-pressure anatexis (cf., Figure 2g). In addition to structural and sedimentary relationships, radiochronometric data testify to related Early Eocene granitoid magmatism, Cenozoic exhumation of domes of lower-terrane gneisses, and Early Cenozoic thermal overprinting of Late Jurassic high-pressure rocks. The almost contiguous distribution of radiometric ages, with little distinction by nominal closure temperature, is compatible with protracted elevated heat flow conditions and a slow general decrease in metamorphic grade in spite of spatial heterogeneities. Much of these characteristics can be produced by delamination in the back-arc position of a retreating subduction zone (Figure 2), where the subjacent asthenosphere serves as source for crustal heating. The present-day depth structure derived from seismic tomography [*Bijwaard et al.*, 1998] exhibits a 300 km segment of subducted lithosphere lying flat on the 670 km discontinuity, a situation which is in accordance with intermediate stages of modeled delamination (Figure 12a: ca. 60 Ma after initiation).

[57] In the Eastern Pontides of NE Turkey, geochemical signatures of adakitic volcanic rocks indicate two ways of melt generation, melting of delaminated eclogitic lowermost crust within subcrustal mantle, and in situ melting of lower crustal rocks exposed to upwelling asthenosphere [*Karsli et al.*, 2010].

[58] High-resolution tomography of the upper mantle across the Alps and the Adria show a wide anomaly of lower P wave velocities indicating strong thinning and delamination of Adria lithosphere [*Giacomuzzi et al.*, 2011].

[59] In and around the Alboran Sea, the notion of subduction and delamination is supported by seismological [*Seber et al.*, 1996; *Calvert et al.*, 2000; *Fullea et al.*, 2010], heat flow [*Polyak et al.*, 1996], present-day extensional kinematic [*Martínez-Martínez et al.*, 2006], and petrological constraints [*Duggen et al.*, 2005]. However, since an at least 60 km thick lithospheric mantle seems to be present everywhere below the Alboran Sea [*Dündar et al.*, 2011], our models do not provide direct analogues to such recent delamination (cf. Figure 2). Three-dimensional effects of a curved plate margin and alternative or supplemental thinning mechanisms such as convective removal may additionally need to be considered [cf. *Valera et al.*, 2008].

[60] A spatial and temporal spread of post-orogenic radiometric records associated with elevated temperature, defining an overall slow cooling, is also reported from the Nampula Province in NE Mozambique [*Bingen et al.*, 2009; *Daszinnies et al.*, 2009; *Macey et al.*, 2010; *Ueda et al.*, 2012], with possible repercussions of delamination up to 300 Ma later [*Emmel et al.*, 2011]. The beginning of the post-collisional tectonic activity falls together with the emplacement of massive non-minimum melt granitoids [*Jacobs et al.*, 2008], post-collisional extension, amphibolite-facies metamorphism, and wide-spread migmatization [*Thomas et al.*, 2010; *Ueda et al.*, 2012].

[61] Post-collisional delamination may account for HT-metamorphism, crustal anatexis, and magmatism that occurs tens of Ma after collision, or in settings that are considered to be anorogenic. It provides a new potential alternative for the generation of anorthosite–mangerite–charnockite–granite magmatic suites (AMCG) whose origin is debated. In Lofoten-Vesterålen (Norway), the majority of magmatic bodies post-dates Svecofennian collision by ca. 60–90 Ma [*Corfu*, 2004]

and granulite-facies metamorphism by ca. 40 Ma [*Griffin et al.*, 1978; *Corfu*, 2004], a timing relationship that could be explained by post-collisional delamination. A delamination setting is compatible with anorthosite formation models in which already molten lower crust (cf. Figures 4f–4h) forms magmas assimilating considerable amounts of depleted granulitic lower crust [e.g., *Schiellerup et al.*, 2000; *Bédard*, 2001]. Delamination could provide a potentially critical heat pulse and would bring asthenosphere to the base of the crust that could account for either a limited or substantial component of mantle melting.

6. Conclusions

[62] Numerical models reproduce delamination without explicit initial weakening of the crust-lithosphere boundary and describe an orogenic cycle from subduction, collision, delamination, collapse and lithospheric recovery. Melting and phase changes are important factors that control initiation and propagation of delamination.

[63] Orogens can undergo delamination from immediately after the onset of collision to long after cessation of relative plate movements. Syn-collisional delamination develops shortly after initial collision while orogens are narrow and cool, in models where activation volumes are low and oceanic slabs are sufficiently old. Delamination initiation predates the development of orogenic characteristics. High activation volumes and low convergence rates form extended orogens that undergo post-collisional delamination more than 100 Ma after collision while orogens are wide and hot, and thickened orogenic crust has already undergone partial melting. Delamination propagates along the crust-mantle boundary as part of upper mantle flow patterns that are to a high degree restricted to the spinel-perovskite transition at 670 km. Delamination is sustained at rates of ca. 0.6–1 cm/a until ca. 600–800 km of subducting plate have been delaminated; thereafter, delamination slows down.

[64] In agreement with previous studies, maxima in topography and local crustal thickening propagate along the subducting plate with the moving delamination front. In the delaminated domain, partial melting is caused or amplified by the opening of a hot asthenospheric window through the lithospheric mantle. Melting is found to be an important factor as it enhances delamination, permits advective heat transport, and increases effective crustal heat flows. The removal of lithospheric mantle is long-lived due to upper mantle flow that maintains high mantle temperatures in the asthenospheric window, hampering renewed growth of lithosphere by cooling. As a consequence, delaminated lithosphere may stay rheologically weak for longer than predicted by static cooling.

Appendix A: Physical Model

A1. Rheological Model

[65] We apply an extended Boussinesq approximation for an incompressible viscous fluid. The simplified stress–strain relationship can be described as

$$\sigma'_{ij} = 2\eta\dot{\varepsilon}_{ij}, \tag{A1}$$

where σ'_{ij} denotes deviatoric stress. The conservative finite difference formulation of the mechanical problem in two dimensions is given by the continuity equation [*Gerya and Yuen*, 2007] for the conservation of mass:

$$\frac{\partial v_x}{\partial x} + \frac{\partial v_z}{\partial z} = -\frac{D\rho}{\rho \cdot Dt}. \tag{A2}$$

[66] For slow creep flow, neglecting inertia, the Stokes equations are

$$\frac{\partial \sigma'_{xx}}{\partial x} + \frac{\partial \sigma'_{xz}}{\partial z} = \frac{\partial P}{\partial x}, \tag{A3}$$

$$\frac{\partial \sigma'_{xz}}{\partial x} + \frac{\partial \sigma'_{zz}}{\partial z} = \frac{\partial P}{\partial z} - g \cdot \rho(T,P,C,M) \tag{A4}$$

for the components of the deviatoric stress tensor. Density is explicitly a function of temperature and pressure (P and T), the given chemical composition (C), and its current phase (melt fraction M).

[67] Strain rate and PT-dependent viscous creep is treated in terms of deformation invariants [*Ranalli*, 1995]. Viscous deformation combines both diffusion and dislocation creep:

$$\frac{1}{\eta_{creep}} = \frac{1}{\eta_{diffusion}} + \frac{1}{\eta_{dislocation}}, \tag{A5}$$

where dislocation creep (and in analogy, diffusion creep with $n = 1$) is calculated as

$$\eta_{dislocation} = \dot{\varepsilon}_{II}^{(1-n)/n} \cdot A^{-1/n} \cdot e^{\left(\frac{E_A + P \cdot V_A}{n \cdot R \cdot T}\right)}, \tag{A6}$$

where $\dot{\varepsilon}_{II} = \sqrt{1/2\dot{\varepsilon}^2_{ij}}$ is the second strain rate invariant, n is the stress exponent, A a material constant, E_A activation energy and V_A activation volume, and R the universal gas constant. Kinematic parameters for the materials as experimentally determined are given with their references in Table 1. Thermodynamically imposed changes of parameters (e.g., change of activation volume as possible grain size comminution during phase change) is not considered. We assume that the transition between creep mechanisms (diffusion and dislocation creep) is smooth and occurs at ca. 0.03 GPa [*Turcotte and Schubert*, 2002].Visco-plastic rheology is obtained by limiting calculated (creep) viscosity according to a plastic yield criterion:

$$\eta_{creep} \leq \frac{c + P \cdot \sin(\phi)}{(4\dot{\varepsilon}_{II})^{1/2}}, \tag{A7}$$

where c is the cohesion of the rock and φ its internal angle of friction. The Peierls mechanism [*Kameyama et al.*, 1999] competes at high pressures with dislocation creep. Peierls creep viscosity η_{Pei} can be expressed as

$$\eta_{Pei} = \frac{1}{2 \cdot A_{Pei} \cdot \sigma_{II}} e^{\left(\frac{E_A + P \cdot V_A}{R \cdot T} \cdot \left(1 - \left[\frac{\sigma_{II}}{\sigma_{Pei}}\right]^m\right)^q\right)}, \tag{A8}$$

where σ_{II}: second stress invariant, and σ_{Pei} is a limiting stress value for the strength of the material. In analogy to dislocation creep, A_{Pei}, m, and q are experimentally

determined material constants. m should range between 0 and 1, whereas q should range between 1 and 2.

[68] The Peierls viscosity is combined with the effective viscosity (to which the Drucker-Prager criterion (equation (A7) has been applied) as a threshold value:

$$\frac{1}{\eta_{eff}} \geq \frac{1}{\eta_{Pei}}. \tag{A9}$$

A2. Heat Conservation, Melting

[69] Lagrangian treatment of the heat equation

$$\rho \cdot C_p \cdot \frac{DT}{Dt} = -\frac{\partial q_x}{\partial x} - \frac{\partial q_z}{\partial z} + H_R + H_A + H_S + H_L \tag{A10}$$

consists of the two-dimensional Fourier law components

$$q_x = -k(T,P,C) \cdot \frac{\partial T}{\partial x}, \tag{A11}$$

$$q_z = -k(T,P,C) \cdot \frac{\partial T}{\partial z}, \tag{A12}$$

and the heat production terms H_R (radiogenic, constant for given composition C) and

$$H_A = T \cdot \alpha \cdot \left(v_x \cdot \frac{\partial P}{\partial x} + v_z \cdot \frac{\partial P}{\partial z} \right), \tag{A13}$$

$$H_S = \sigma'_{xx} \cdot \dot{\varepsilon}_{xx} + \sigma'_{zz} \cdot \dot{\varepsilon}_{zz} + 2\sigma'_{xz} \cdot \dot{\varepsilon}_{xz}, \tag{A14}$$

for the adiabatic (H_A) and shear (H_S) heat production. Latent heat production H_L due to phase changes ΔM is implicitly accounted for by modification of effective heat capacity and thermal expansion coefficient [*Burg and Gerya*, 2005]:

$$C_{p,eff} = C_{p,0} + H_L \cdot \left(\frac{\partial M}{\partial T} \right)_{P=const}, \tag{A15}$$

$$\alpha_{eff} = \alpha_0 + \rho \cdot \frac{H_L}{T} \cdot \left(\frac{\partial M}{\partial P} \right)_{T=const}, \tag{A16}$$

where $C_{p,\,0}$ and α_0 are properties for the solid phase and H_L is the (constant) latent heat for the complete melting/solidification of a given material as listed in Table 1.

[70] Melting (volumetric degree) is modeled as a function of both temperature and pressure linearly increasing [*Schmidt and Poli*, 1998] between solidus $T_{sol}(P)$ and liquidus $T_{liq}(P)$ (see Table 1):

$$M = \begin{cases} 0 & \text{for} \quad T \leq T_{sol} \\ \dfrac{T - T_{sol}}{T_{liq} - T_{sol}} & \text{for} \quad T_{sol} < T < T_{liq} \\ 1 & \text{for} \quad T \geq T_{liq} \end{cases}. \tag{A17}$$

Fractions of melts are not extracted from partially molten rocks in this study, as opposed to e.g., *Sizova et al.* [2010]. Melting is not modeled below a depth of 400 km.

A3. Material Conversion: Erosion/Sedimentation, Hydration

[71] Material conversion due to surface processes are implemented using a gross erosion/sedimentation law where the interface $z_{e,s}$ between rocks and air/water is tracked on markers. Material is eroded or sedimented (marker type conversion) with reference to an erosion and sedimentation level l_0 as a function of grid velocities according to

$$\frac{\partial z_{e,s}}{\partial t} = v_z - v_x \cdot \frac{\partial z_{e,s}}{\partial x} - v_s + v_e, \tag{A18}$$

where v_x, v_z are the velocity components interpolated from the Eulerian grid, and v_e, v_s are the rates for mutually exclusive erosion and sedimentation depending on whether $z_{e,s} > < l_0$. The reference level l_0 is at 10 km throughout the study; unless otherwise noted, both v_e and v_s are 0.1 mm/a.

[72] Water is both present within hydrous minerals when thermodynamically stable, and as depth-dependent pore water. Water content (%) reflecting compaction as a function of depth below surface, Δz [km], is represented as

$$X_{H_2O} = X_{H_2O,\rho_0} \cdot \left(1 - \frac{\Delta z}{75} \right), \tag{A19}$$

decreasing linearly from a connate water content of X_{H_2O,ρ_0} = 2 wt.% at the surface. Dehydration assuming thermodynamic equilibrium is predicted from the petrological model following minimization of Gibbs free energy and represented by generation of a fluid marker accounting for the amount of released water. Fluid markers for free excess water, predicted as stable phase, are moved in the velocity field until coinciding with a lithology which is capable to hydrate under given PT conditions. A fixed upward percolation velocity for free water in the mantle v_{perc} of 10 mm/a is superimposed on the velocity field, such that

$$v_{x,H_2O} = v_x, \tag{A20}$$

$$v_{y,H_2O} = v_y - v_{perc}. \tag{A21}$$

A4. Implementation of Initial Convergence

[73] Initial convergence is prescribed in both continental plates until the complete oceanic plate has been consumed, representing assumed external plate forces. The respective horizontal velocities are set at two vertical strips (1 node wide) of internal boundary nodes, located at 1000 km and 3000 km, and reaching from 10 km to 70 km in depth. Transmission is ensured by stiffening the stripes and immediately adjacent nodes in all directions (i.e., 3 nodes wide high-viscosity stripes of 10^{26} Pa · s). Thereby the velocities are effectively imposed on all rheologically strong portions of the plate, and do not rely on coupling between crust and lithospheric mantle. Together with lateral free-slip conditions, this leads to upwards flow of mantle material along the boundaries to balance the resulting local mass deficit.

A5. Surface Predictions

[74] Heat flow is calculated over grid cells using physical properties updated on the adjacent nodes of the staggered grid as

$$q_z = \frac{\Delta T}{\Delta z} \cdot \left(\frac{k_{(i)} + k_{(i+1)}}{2} \right), \tag{A22}$$

where

$$k = \left(c_1 + \frac{c_2}{T + 77} \right) \cdot e^{(c_3 \cdot P)}, \tag{A23}$$

where T, P are temperature and pressure in [K] and [MPa] respectively, and $c_{1 \ldots 3}$ are empirical material constants given in Table 1. Surface heat flow is predicted from the interpolation of the surface to the next lower Eulerian grid node, and consideration of the calculated heat flow value at the lower cell (or $+\frac{1}{2}\Delta z$ staggered node) neighboring the surface node, i.e., $q(i) \sim q(i + 1/2)$, such that physical properties of supra-surface materials are excluded from the calculation.

[75] **Acknowledgments.** T. Duretz, J. Jacobs, F. Corfu, C. Thieulot, S. Jammes, and the members of the DELAM project are thanked for helpful suggestions and interesting discussions. K.U. was supported by NFR grant 177514 and the University of Bergen. This work was also supported by ETH research grant ETH-0609-2, SNF research grants 200020–126832, 200020–129487, SNF ProDoc program 4-D-Adamello, TopoEurope program, and Crystal2Plate program. Constructive and valuable comments by A. Negredo, H. Schmeling, and an Associate Editor are gratefully acknowledged.

References

Bajolet, F., J. Galeano, F. Funiciello, M. Moroni, A. M. Negredo, and C. Faccenna (2012), Continental delamination: Insights from laboratory models, *Geochem. Geophys. Geosyst.*, *13*, Q02009, doi:10.1029/2011GC003896.

Bakun-Czubarov, N. (1991), On the possibility of occurrence of quartz pseudomorphs after coesite in the eclogite–granulite rock series of the Złote Mountains in the Sudetes (SW Poland), *Arch. Mineral.*, *42*, 5–16.

Baumann, C., T. V. Gerya, and J. A. D. Connolly (2010), Numerical modelling of spontaneous slab breakoff dynamics during continental collision, *Geol. Soc. Spec. Publ.*, *332*, 99–114, doi:10.1144/SP332.7.

Bédard, J. H. (2001), Parental magmas of the Nain Plutonic Suite anorthosites and mafic cumulates: A trace element modelling approach, *Contrib. Mineral. Petrol.*, *141*, 747–771, doi:10.1007/s004100100268.

Bijwaard, H., W. Spakman, and E. R. Engdahl (1998), Closing the gap between regional and global travel time tomography, *J. Geophys. Res.*, *103*(B12), 30,055–30,078, doi:10.1029/98JB02467.

Bingen, B., J. Jacobs, G. Viola, I. H. C. Henderson, Ø. Skår, R. Boyd, R. J. Thomas, A. Solli, R. M. Key, and E. X. F. Daudi (2009), Geochronology of the Precambrian crust in the Mozambique belt in NE Mozambique, and implications for Gondwana assembly, *Precambrian Res.*, *170*, 231–255, doi:10.1016/j.precamres.2009.01.005.

Bird, P. (1979), Continental delamination and the Colorado Plateau, *J. Geophys. Res.*, *84*, 7561–7571.

Bird, P., and J. Baumgardner (1981), Steady propagation of delamination events, *J. Geophys. Res.*, *86*(B6), 4891–4903, doi:10.1029/JB086iB06p04891.

Bittner, D., and H. Schmeling (1995), Numerical modeling of melting processes and induced diapirism in the lower crust, *Geophys. J. Int.*, *123*, 59–70, doi:10.1111/j.1365-246X.1995.tb06661.x.

Boutelier, D., A. Chemenda, and C. Jorand (2004), Continental subduction and exhumation of high-pressure rocks: Insights from thermo-mechanical laboratory modelling, *Earth Planet. Sci. Lett.*, *222*, 209–216, doi:10.1016/j.epsl.2004.02.013.

Brown, C. D., and R. J. Phillips (2000), Crust–mantle decoupling by flexure of continental lithosphere, *J. Geophys. Res.*, *105*, 13,221–13,237, doi:10.1029/2000JB900069.

Burg, J.-P. (2012), Rhodope: From Mesozoic convergence to Cenozoic extension. Review of petro-structural data in the geochronological frame, in *The Geology of Greece*, edited by E. Skourtsos and G. S. Lister, *J. Virtual Explor.*, *42*, 1–44, doi:10.3809/jvirtex.2011.00270.

Burg, J.-P., and T. V. Gerya (2005), The role of viscous heating in Barrovian metamorphism of collisional orogens: Thermomechanical models and application to the Lepontine Dome in the central Alps, *J. Metamorph. Geol.*, *23*, 75–95, doi:10.1111/j.1525-1314.2005.00563.x.

Burov, E., and S. Cloetingh (2010), Plume-like upper mantle instabilities drive subduction initiation, *Geophys. Res. Lett.*, *37*, L03309, doi:10.1029/2009GL041535.

Calvert, A., E. Sandvol, D. Seber, M. Barazangi, S. Roecker, T. Mourabit, F. Vidal, G. Alguacil, and N. Jabour (2000), Geodynamic evolution of the lithosphere and upper mantle beneath the Alboran region of the western Mediterranean: Constraints from travel time tomography, *J. Geophys. Res.*, *105*(B5), 10,871–10,898, doi:10.1029/2000JB900024.

Channell, J. E. T., and J. C. Mareschal (1989), Delamination and asymmetric lithospheric thickening in the development of the Tyrrhenian Rift, *Geol. Soc. Spec. Publ.*, *45*, 285–302, doi:10.1144/GSL.SP.1989.045.01.16.

Chopin, C. (1984), Coesite and pure pyrope in high-grade blueschists of the Western Alps: A first record and some consequences, *Contrib. Mineral. Petrol.*, *86*, 107–118, doi:10.1007/BF00381838.

Chopin, C. (2003), Ultrahigh-pressure metamorphism: Tracing continental crust into the mantle, *Earth Planet. Sci. Lett.*, *212*, 1–14, doi:10.1016/S0012-821X(03)00261-9.

Clauser, C., and E. Huenges (1995), Thermal conductivity of rocks and minerals, in *Rock Physics and Phase Relations*, *AGU Ref. Shelf*, vol. 3, edited by T. J. Ahrens, pp. 105–126, AGU, Washington, D. C.

Cloetingh, S. A. P. L., M. J. R. Wortel, and N. J. Vlaar (1982), Evolution of passive continental margins and initiation of subduction zones, *Nature*, *297*, 139–142, doi:10.1038/297139a0.

Conrad, C. P. (2000), Convective instability of thickening mantle lithosphere, *Geophys. J. Int.*, *143*, 52–70, doi:10.1046/j.1365-246x.2000.00214.x.

Conrad, C. P., and C. Lithgow-Bertelloni (2002), How mantle slabs drive plate tectonics, *Science*, *298*, 207–209, doi:10.1126/science.1074161.

Conrad, C. P., and C. Lithgow-Bertelloni (2006), Influence of continental roots and asthenosphere on plate-mantle coupling, *Geophys. Res. Lett.*, *33*, L05312, doi:10.1029/2005GL025621.

Cook, F. A., A. J. van der Velden, K. W. Hall, and B. J. Roberts (1998), Tectonic delamination and subcrustal imbrication of the Precambrian lithosphere in northwestern Canada mapped by LITHOPROBE, *Geology*, *26*, 839–842, doi:10.1130/0091-7613(1998)026<0839:TDASIO>2.3.CO;2.

Corfu, F. (2004), U–Pb age, setting and tectonic significance of the anorthosite–mangerite–charnockite–granite suite, Lofoten–Vesterålen, Norway, *J. Petrol.*, *45*, 1799–1819, doi:10.1093/petrology/egh034.

Crameri, F., H. Schmeling, G. J. Golabek, T. Duretz, R. Orendt, S. J. H. Buiter, D. A. May, B. J. P. Kaus, T. V. Gerya, and P. J. Tackley (2012), A comparison of numerical surface topography calculations in geodynamic modelling: An evaluation of the 'sticky air' method, *Geophys. J. Int.*, *198*, 38–54, doi:10.1111/j.1365-246X.2012.05388.x.

Daszinnies, M. C., J. Jacobs, J. A. Wartho, and G. H. Grantham (2009), Post Pan-African thermo-tectonic evolution of the north Mozambican basement and its implication for the Gondwana rifting. Inferences from $^{40}Ar/^{39}Ar$ hornblende, biotite and titanite fission-track dating, *Geol. Soc. Spec. Publ.*, *324*, 261–286, doi:10.1144/SP324.18.

Duggen, S., K. Hoernle, P. van den Bogaard, and D. Garbe-Schönberg (2005), Post-collisional transition from subduction to intraplate-type magmatism in the westernmost Mediterranean: Evidence for continental-edge delamination of subcontinental lithosphere, *J. Petrol.*, *46*, 1155–1201, doi:10.1093/petrology/egi013.

Dündar, S., et al. (2011), Receiver function images of the base of the lithosphere in the Alboran Sea region, *Geophys. J. Int.*, *187*, 1019–1026, doi:10.1111/j.1365-246X.2011.05216.x.

Duretz, T., T. V. Gerya, and D. A. May (2011), Numerical modelling of spontaneous slab breakoff and subsequent topographic response, *Tectonophysics*, *502*, 244–256, doi:10.1016/j.tecto.2010.05.024.

Durham, W. B., S. Mei, D. L. Kohlsted, L. Wang, and N. A. Dixon (2009), New measurements of activation volume in olivine under anhydrous conditions, *Phys. Earth Planet. Inter.*, *172*, 67–73, doi:10.1016/j.pepi.2008.07.045.

Ellis, M. (1988), Lithospheric strength in compression; initiation of subduction, flake tectonics, foreland migration of thrusting, and an origin of displaced terranes, *J. Geol.*, *96*, 91–100, doi:10.1086/629195.

Emmel, B., R. Kumar, K. Ueda, J. Jacobs, M. C. Daszinnies, R. J. Thomas, and R. Matola (2011), Thermochronological history of an orogen-passive margin system–an example from N Mozambique, *Tectonics*, *30*, TC2002, doi:10.1029/2010TC002714.

Evans, A. G., and J. W. Hutchinson (1984), On the mechanics of delamination and spalling in compressed films, *Int. J. Solids Struct.*, *20*, 455–466, doi:10.1016/0020-7683(84)90012-X.

Faccenda, M., G. Minelli, and T. Gerya (2009), Numerical modeling of active advancing and retreating post-subduction collision controlled by rheological weakening of the subduction channel, *Earth Planet. Sci. Lett.*, *278*, 337–349, doi:10.1016/j.epsl.2008.12.021.

Fullea, J., M. Fernandez, J. C. Afonso, J. Verges, and H. Zeyen (2010), The structure and evolution of the lithosphere-asthenosphere boundary beneath the Atlantic-Mediterranean transition region, *Lithos*, *120*, 74–95, doi:10.1016/j.lithos.2010.03.003.

Gerya, T. V., and D. A. Yuen (2003), Characteristics-based marker-in-cell method with conservative finite-differences schemes for modelling geological flows with strongly variable transport properties, *Phys. Earth Planet. Inter.*, *140*, 293–318, doi:10.1016/j.pepi.2003.09.006.

Gerya, T. V., and D. A. Yuen (2007), Robust characteristics method for modelling multiphase visco-elasto-plastic thermo-mechanical problems, *Phys. Earth Planet. Inter.*, *163*, 83–105, doi:10.1016/j.pepi.2007.04.015.

Gerya, T., D. A. Yuen, and W. V. Maresch (2004), Thermomechanical modelling of slab detachment, *Earth Planet. Sci. Lett.*, *226*, 101–116, doi:10.1016/j.epsl.2004.07.022.

Gerya, T. V., L. L. Perchuk, and J.-P. Burg (2008), Transient hot channels: Perpetrating and regurgitating ultrahigh-pressure, high temperature crust-mantle associations in collision belts, *Lithos*, *103*, 236–256, doi:10.1016/j.lithos.2007.09.017.

Giacomuzzi, G., C. Chiarabba, and P. De Gori (2011), Linking the Alps and Apennines subduction systems: New constraints revealed by high-resolution teleseismic tomography, *Earth Planet. Sci. Lett.*, *301*, 531–543, doi:10.1016/j.epsl.2010.11.033.

Göğüs, O., and R. N. Pysklywec (2008a), Near-surface diagnostics of dripping or delaminating lithosphere, *J. Geophys. Res.*, *113*, B11404, doi:10.1029/2007JB005123.

Göğüs, O., and R. N. Pysklywec (2008b), Mantle lithosphere delamination driving plateau uplift and synconvergent extension in eastern Anatolia, *Geology*, *36*, 723–726, doi:10.1130/G24982A.1.

Göğüs, O., R. N. Pysklywec, F. Corbi, and C. Faccenna (2011), The surface tectonics of mantle lithosphere delamination following ocean lithosphere subduction: Insights from physical-scaled analogue experiments, *Geochem. Geophys. Geosyst.*, *12*, Q05004, doi:10.1029/2010GC003430.

Gray, R., and R. N. Pysklywec (2012), Geodynamic models of mature continental collision: Evolution of an orogen from lithospheric subduction to continental retreat/delamination, *J. Geophys. Res.*, *117*, B03408, doi:10.1029/2011JB008692.

Griffin, W. L., P. N. Taylor, J. W. Hakkinen, K. S. Heier, I. K. Iden, E. J. Krogh, O. Malm, K. I. Olsen, D. E. Ormaasen, and E. Tveten (1978), Archaean and Proterozoic crustal evolution in Lofoten–Vesteralen, N Norway, *J. Geol. Soc.*, *135*, 629–647, doi:10.1144/gsjgs.135.6.0629.

Guillaume, B., M. Moroni, F. Funiciello, J. Martinod, and C. Faccena (2010), Mantle flow and dynamic topography associated with slab window opening: Insights from laboratory models, *Tectonophysics*, *496*, 83–98, doi:10.1016/j.tecto.2010.10.014.

Hacker, B. R., L. Ratschbacher, L. Webb, M. O. McWilliams, T. Ireland, A. Calvert, S. Dong, H.-R. Wenk, and D. Chateigner (2000), Exhumation of ultrahigh-pressure continental crust in east central China: Late Triassic-Early Jurassic tectonic unroofing, *J. Geophys. Res.*, *105*, 13,339–13,364, doi:10.1029/2000JB900039.

Hermann, J., D. Rubatto, A. Korsakov, and V. S. Shatsky (2001), Multipe zircon growth during fast exhumation of diamondiferous, deeply subducted continental crust (Kokchetav Massif, Kazahkhstan), *Contrib. Mineral. Petrol.*, *141*, 66–82, doi:10.1007/s004100000218.

Houseman, G. A., and P. Molnar (1997), Gravitational (Rayleigh-Taylor) instability of a layer with non-linear viscosity and convective thinning of continental lithosphere, *Geophys. J. Int.*, *128*, 125–150, doi:10.1111/j.1365-246X.1997.tb04075.x.

Houseman, G. A., D. P. McKenzie, and P. Molnar (1981), Convective instability of a thickened boundary layer and its relevance for the thermal evolution of continental convergence belts, *J. Geophys. Res.*, *86*, 6115–6132, doi:10.1029/JB086iB07p06115.

Jacobs, J., B. Bingen, R. J. Thomas, W. Bauer, M. Wingate, and P. Feitio (2008), Early Palaeozoic orogenic collapse and voluminous late-tectonic magmatism in Dronning Maud Land and Mozambique: Insights into the partially delaminated orogenic root of the East African-Antarctic Orogen?, *Geol. Soc. Spec. Publ.*, *308*, 69–90, doi:10.1144/SP308.3.

Kameyama, M., D. A. Yuen, and S.-I. Karato (1999), Thermal–mechanical effects of low-temperature plasticity (the peierls mechanism) on the deformation of viscoelastic shear zone, *Earth Planet. Sci. Lett.*, *168*, 159–172, doi:10.1016/S0012-821X(99)00040-0.

Karsli, O., A. Dokkuz, A. Uysal, F. Aydin, R. Kandemir, and J. Wijbrans (2010), Generation of the Early Cenozoic adakitic volcanism by partial melting of mafic lower crust, eastern Turkey: Implications for crustal thickening to delamination, *Lithos*, *114*, 109–120, doi:10.1016/j.lithos.2009.08.003.

Kay, R. W., and S. M. Kay (1993), Delamination and delamination magmatism, *Tectonophysics*, *219*, 177–189, doi:10.1016/0040-1951(93)90295-U.

King, S. D., and D. L. Anderson (1998), Edge-driven convection, *Earth Planet. Sci. Lett.*, *160*, 289–296, doi:10.1016/S0012-821X(98)00089-2.

Kotkova, J., P. J. O'Brien, and M. A. Ziemann (2011), Diamond and coesite discovered in Saxony-type granulite: Solution to the Variscan garnet peridotite enigma, *Geology*, *39*, 667–670, doi:10.1130/G31971.1.

Kusznir, N. J., and R. G. Park (1986), Continental lithosphere strength: The critical role of lower crustal deformation, *Geol. Soc. Spec. Publ.*, *24*, 79–93, doi:10.1144/GSL.SP.1986.024.01.09.

Lappin, M. A., and D. C. Smith (1978), Mantle-equilibrated orthopyroxene eclogite pods from the basal gneisses in the Selje district, western Norway, *J. Petrol.*, *19*, 530–584.

Leech, M. L. (2001), Arrested orogenic development: Eclogitization, delamination, and tectonic collapse, *Earth Planet. Sci. Lett.*, *185*, 149–159, doi:10.1016/S0012-821X(00)00374-5.

Macey, P. H., et al. (2010), Mesoproterozoic geology of the Nampula Block, northern Mozambique: Tracing fragments of Mesoproterozoic crust in the heart of Gondwana, *Precambrian Res.*, *182*, 124–148, doi:10.1016/j.precamres.2010.07.005.

Martínez-Martínez, J. M., B.-R. Guillermo, J. M. Azanon, and F. Torcal (2006), Active transfer fault zone linking a segmented extensional system (Betics, southern Spain): Insight into heterogeneous extension driven by edge delamination, *Tectonophysics*, *422*, 159–173, doi:10.1016/j.tecto.2006.06.001.

Mei, S., and D. L. Kohlstedt (2000), Influence of water on plastic deformation of olivine aggregates: 2. Dislocation creep regime, *J. Geophys. Res.*, *105*(B9), 21,471–21,481, doi:10.1029/2000JB900180.

Meissner, R., and W. Mooney (1998), Weakness of the lower continental crust: A condition for delamination, uplift, and escape, *Tectonophysics*, *296*, 47–60, doi:10.1016/S0040-1951(98)00136-X.

Moore, V. M., and D. V. Wiltschko (2004), Syncollisional delamination and tectonic wedge development in convergent orogens, *Tectonics*, *23*, TC2005, doi:10.1029/2002TC001430.

Morency, C., and M.-P. Doin (2004), Numerical simulations of mantle lithospheric delamination, *J. Geophys. Res.*, *109*, B03410, doi:10.1029/2003JB002414.

Nelson, K. D. (1992), Are crustal thickness variations in old mountain belts like the Appalachians a consequence of lithospheric delamination?, *Geology*, *20*, 498–502, doi:10.1130/0091-7613(1992)020<0498:ACTVIO>2.3.CO;2.

Nikolaeva, K., T. Gerya, and F. Marques (2010), Subduction initiation at passive margins: Numerical modeling, *J. Geophys. Res.*, *115*, B03406, doi:10.1029/2009JB006549.

Polyak, B. G., et al. (1996), Heat flow in the Alboran Sea, western Mediterranean, *Tectonophysics*, *263*, 191–218.

Poudjom Djomani, Y. H., S. Y. O'Reilly, W. L. Griffin, and P. Morgan (2001), The density structure of subcontinental lithosphere through time, *Earth Planet. Sci. Lett.*, *184*, 605–621, doi:10.1016/S0012-821X(00)00362-9.

Ranalli, G. (1995), *Rheology of the Earth*, Chapman and Hall, London.

Regenauer-Lieb, K., D. A. Yuen, and J. Branlund (2001), The initiation of subduction: Criticality by addition of water?, *Science*, *294*, 578–580, doi:10.1126/science.1063891.

Rey, P. (2001), From lithospheric thickening and divergent collapse to active continental rifting, *Geol. Soc. Spec. Publ.*, *184*, 77–88, doi:10.1144/GSL.SP.2001.184.01.05.

Rey, P., J.-P. Burg, and M. Casey (1997), The Scandinavian Caledonides and their relationship to the Variscan belt, *Geol. Soc. Spec. Publ.*, *121*, 179–200, doi:10.1144/GSL.SP.1997.121.01.08.

Sacks, P. E., and D. T. Secor (1990), Delamination in collisional orogens, *Geology*, *18*, 999–1002, doi:10.1130/0091-7613(1990)018<0999:DICO>2.3.CO;2.

Saleeby, J., and Z. Foster (2004), Topographic response to mantle lithosphere removal in the southern Sierra Nevada region, *Calif. Geol.*, *32*, 245–248.

Schiellerup, H., R. D. Lambert, T. Prestvik, B. Robins, J. McBride, and R. B. Larsen (2000), Re-Os isotopic evidence for a lower crustal origin of massif-type anorthosites, *Nature*, *405*, 781–784, doi:10.1038/35015546.

Schmeling, H., et al. (2008), A benchmark comparison of spontaneous subduction model—Towards a free surface, *Phys. Earth Planet. Inter.*, *171*, 198–223, doi:10.1016/j.pepi.2008.06.028.

Schmidt, M. W., and S. Poli (1998), Experimentally based water budgets for dehydrating slabs and consequences for arc magma generation, *Earth Planet. Sci. Lett.*, *163*, 361–379, doi:10.1016/S0012-821X(98)00142-3.

Schott, B., and H. Schmeling (1998), Delamination and detachment of a lithospheric root, *Tectonophysics*, *296*, 225–247, doi:10.1016/S0040-1951(98)00154-1.

Schott, B., D. Yuen, and H. Schmeling (2000), The significance of shear heating in continental delamination, *Phys. Earth Planet. Inter.*, *118*, 273–290, doi:10.1016/S0031-9201(99)00159-4.

Seber, D., M. Barazangi, A. Ibenbrahim, and A. Demnati (1996), Geophysical evidence for lithospheric delamination beneath the Alboran Sea and Rif-Betic mountains, *Nature*, *379*, 785–790, doi:10.1038/379785a0.

Seno, T. (2008), Conditions for a crustal block to be sheared off from the subducted continental lithosphere: What is an essential factor to cause features associated with collision?, *J. Geophys. Res.*, *113*, B04414, doi:10.1029/2007JB005038.

Shatsky, V. S., E. Jagoutz, N. V. Sobolev, O. A. Kozmenko, V. S. Parkhomenko, and M. Troesch (1999), Geochemistry and age of ultrahigh pressure metamorphic rocks from the Kokchetav massif (northern Kazakhstan), *Contrib. Mineral. Petrol.*, *137*, 185–205, doi:10.1007/s004100050545.

Sizova, E., T. V. Gerya, M. Brown, and L. L. Perchuk (2010), Subduction styles in the Precambrian: Insight from numerical experiments, *Lithos*, *116*, 209–229, doi:10.1016/j.lithos.2009.05.028.

Sperner, B., D. Ioane, and R. J. Lillie (2004), Slab behaviour and its surface expression: New insights from gravity modelling in the SE-Carpathians, *Tectonophysics*, *382*, 51–84, doi:10.1016/j.tecto.2003.12.008.

Spohn, T., and G. Schubert (1982), Convective thinning of the lithosphere: A mechanism for the initiation of continental rifting, *J. Geophys. Res.*, *87*, 4669–4681, doi:10.1029/JB087iB06p04669.

Tackley, P. J. (2008), Layer cake or plum pudding?, *Nat. Geosci.*, *1*, 157–158, doi:10.1038/ngeo134.

Thomas, R. J., J. Jacobs, M. S. A. Horstwood, K. Ueda, B. Bingen, and R. Matola (2010), The Mecubúri and Alto Benfica Groups, NE Mozambique: Aids to unravelling ca. 1 and 0.5 Ga events in the East African Orogen, *Precambrian Res.*, *178*, 72–90, doi:10.1016/j.precamres.2010.01.010.

Tsumura, N., H. Ikawa, T. Ikawa, M. Shinohara, T. Ito, K. Arita, T. Moriya, G. Kimura, and T. Ikawa (1999), Delamination-wedge structure beneath the Hidaka Collision Zone, central Hokkaido, Japan inferred from seismic reflection profiling, *Geophys. Res. Lett.*, *26*, 1057–1060, doi:10.1029/1999GL900192.

Turcotte, D. L., and G. Schubert (2002), *Geodynamics*, Cambridge Univ. Press, Cambridge, U. K.

Ueda, K., T. Gerya, and S. V. Sobolev (2008), Subduction initiation by thermal–chemical plumes: Numerical studies, *Phys. Earth Planet. Inter.*, *171*(1–4), 296–312, doi:10.1016/j.pepi.2008.06.032.

Ueda, K., J. Jacobs, R. J. Thomas, J. Kosler, F. Jourdan, and R. Matola (2012), Delamination-induced late tectonic deformation and high-grade metamorphism of the Proterozoic Nampula Complex, northern Mozambique, *Precambrian Res.*, *196–197*, 275–294, doi:10.1016/j.precamres.2011.05.012.

Valera, J. L., A. M. Negredo, and A. Villaseñor (2008), Asymmetric delamination and convective removal numerical modeling: Comparison with evolutionary models for the Alboran Sea region, *Pure Appl. Geophys.*, *165*, 1683–1706, doi:10.1007/s00024-008-0395-8.

Valera, J. L., A. M. Negredo, and I. Jimenez-Munt (2011), Deep and near-surface consequences of root removal by asymmetric continental delamination, *Tectonophysics*, *502*, 257–265, doi:10.1016/j.tecto.2010.04.002.

Vanderhaeghe, O. (2009), Migmatites, granites and orogeny: Flow modes of partially molten rocks and magmas associated with melt/solid segregation in orogenic belts, *Tectonophysics*, *477*, 119–134, doi:10.1016/j.tecto.2009.06.021.

Wallner, H., and H. Schmeling (2010), Rift induced delamination of mantle lithosphere and crustal uplift: A new mechanism for explaining Rwenzori Mountains' extreme elevation?, *Int. J. Earth Sci.*, *99*, 1511–1524, doi:10.1007/s00531-010-0521-6.

Wallner, H., and H. Schmeling (2011), Sensitivity analysis of rift induced delamination with application to Rwenzori Mountains, *Geophys. J. Int.*, *187*, 1135–1145, doi:10.1111/j.1365-246X.2011.05237.x.

Warren, C. J., C. Beaumont, and R. A. Jamieson (2008), Modelling tectonic styles and ultra-high pressure (UHP) rock exhumation during the transition from oceanic subduction to continental collision, *Earth Planet. Sci. Lett.*, *267*, 129–145, doi:10.1016/j.epsl.2007.11.025.

Wyllie, P. J. (1988), Magma genesis, plate tectonics, and chemical differentiation of the Earth, *Rev. Geophys.*, *26*, 370–404, doi:10.1029/RG026i003p00370.

Xu, S., W. Su, Y. Liu, L. Jiang, S. Ji, I. Okay, and A. M. C. Sengör (1992), Diamond from the Dabie Shan metamorphic rocks and its implications for tectonic setting, *Science*, *256*, 80–82, doi:10.1126/science.256.5053.80.